Modelling of sulphuric acid aerosols in an engine plume

Using one-way-coupled turbulent diffusivity and appropriate microphysical models

MSc. Thesis Aerospace Engineering

Tluk A.J.

Delft University of Technology

TU Delft

Modelling of sulphuric acid aerosols in an engine plume

Using one-way-coupled turbulent diffusivity and appropriate microphysical models

by

Tluk A.J.

Student Name	Student Number
Tluk A.J.	4111613

Supervisors:	Dr. S.J. Hulshoff MSc. I.E. de Vries MSc. M. Janssens
Thesis Committee:	Dr. S.J. Hulshoff Dr. B.W. van Oudheusden Dr. I.C. Dedoussi
Faculty:	Faculty of Aerospace Engineering, Delft

Cover: Arno Senoner (2020)

TU Delft

***To Mom*.**

Acknowledgements

I would like to express my heartfelt gratitude and appreciation to the following individuals whose unwavering support and guidance have played a crucial role in the successful completion of my thesis. First and foremost, I am deeply indebted to my supervisor, Dr. Steven Hulshoff, for their invaluable mentorship throughout my research journey. I would also like to extend my sincere thanks to Iris de Vries and Martin Janssens whose willingness to spare time, share their knowledge, and offer constructive criticism greatly enriched my research experience and contributed significantly to the overall outcome of this work. Additionally, I am grateful to Dr. Colleen Golja, whose generosity in providing me with access to her software proved invaluable in conducting the necessary analyses for this study. I would like to express my deepest appreciation to Maaike, for their unwavering support, understanding, and encouragement throughout. I would also like to extend my gratitude to Bodo, for their guidance in maintaining my mental well-being and ensuring the completion of this work. Finally, I would like to acknowledge my father, Karel, whom without none of this would have been possible in the first place.

Tluk A.J.
Delft, July 2023

Summary

This research focuses on gaining a better understanding of the formation, growth, and size distribution of H_2SO_4 aerosols in the first seconds after injection within an aircraft engine plume. The study aims to enhance the fidelity of calculations by incorporating spatial variation, which is more representative of real-world scenarios. The research objectives include developing a toolchain using the available AER 3-D software, setting up a computational fluid dynamics (CFD) model of an engine wake using GSP Engine model as inputs, designing a model for one-way coupling the results of the CFD flow field with microphysics and an advection scheme.

The research begins by comparing the AER 3-D microphysics model to two state-of-the-art box models used in previous studies. To do so however, the flow field needs to be adjusted to reproduce their spatial simplifications. The toolchain is therefore applied to quasi 1-D (Q1-D) domains. This Q1-D approach is first validated by comparing a Q1-D equivalent of SCoPEx experiment to its 3-D results and show comparable results. The box models are used for validation to see if it can reproduce the trend of aerosol growth with high initial concentrations and diffusivity. The results indicate that the AER 3-D model, can handle high initial concentrations of H_2SO_4 and produces similar number-mean radius and size distribution results compared to the validation data.

To further evaluate the effects of realistic engine conditions, an axisymmetric engine wake field is calculated using ANSYS with the boundary conditions defined by the outputs of a GSP engine model, and the growth rates and size distributions of aerosols are analysed. The results show that condensation and nucleation mainly occur in the injection area and wake boundary layer, while coagulation primarily happens inside the wake. Additionally, the presence of turbulence influences the diffusion and growth of aerosols, leading to variations in particle size as a function of distance from the center of the wake.

The research concludes that incorporating spatial variation and turbulence modelling is crucial for accurately predicting aerosol behaviour. The study highlights the importance of coupling CFD with microphysics and the advection scheme and provides insights into the influence of flow parameters and initial concentrations on aerosol size distribution. Suggestions for future research include conducting sensitivity studies, investigating more accurate input conditions, and exploring additional microphysical routines. Furthermore, the complexity of the CFD can be increased and microphysics models can be increased to incorporate ion-induced effects and heterogenous microphysical calculations.

Contents

Nomenclature

Abbreviations

Abbreviation	Definition
AER	Atmospheric and Environmental Research
BC	Boundary Condition
CFD	Computational Fluid Dynamics
DNS	Direct Numerical Simulation
EVM	Eddy Viscosity Model
GHG	Greenhouse Gases
GSP	Gas Turbine Simulation Program
IC	Initial Concentration
IR	Injection Rate
ISA	International Standard Atmosphere
IV	Injection Volume
LES	Large Eddy Simulation
NMPR	Number-Median Particle Radius
NOD	Number Off Divisions
N-S	Navier-Stokes
Q1-D	Quasi One Dimensional
RANS	Reynolds-Averaged Navier-Stokes
RF	Radiative Forcing
RSM	Reynolds’ Stress Model
SAI	Stratospheric Aerosol Injection
SGS	Sub-Grid Scale
SRM	Solar Radiation Management
SST	Shear Stress Transport
TOMAS	TwO-Moment Aerosol Sectional
VMD	Volume-Mean Radius

Symbols

Symbol	Definition	Unit
B	Mobility	[s kg^{-1}]
C	Kinetic threshold	[cm^{-3}]
C_D	Turbulence model calibration constant	[-]
D	Diffusion coefficient	[-]
D	Bulk density	[g cm^{-3}]
G	Average kinetic velocity	[m s^{-1}]
G	Gibbs free energy	[J]
ΔG	Gibbs free energy saddle point value	[J]
J	Nucleation rate	[cm^{-3} s^{-1}]
k	Turbulent kinetic energy	[cm^2 s^{-2}]
k	Boltzmann constant	[JK^{-1}]
K_{ij}	Coagulation kernel	[cm^3 s^{-1}]
Kn	Knudsen number	[-]
l_{eff}	Effective mean free path	[μm]
l_m	Mixing length	[m]
M	Mass	[g]
M_i	Molecular weight	[g mol^{-1}]
N	number density	[cm^{-3}]
P	Pressure	[Pa]
P^0	Equilibrium vapour pressure	[Pa]
Pr	Prandtl number	[-]
r	Radius	[μm]
R	Universal gas constant	[J K^{-1} mol^{-1}]
r^*	Radius of critical embryo	[nm]
Re	Reynolds number	[-]
T	Temperature	[K]
t	Time	[s]
T_e	Equilibrium temperature	[K]
u, v, w	Velocity	[m s^{-1}]
$\bar{u}, \bar{v}, \bar{w}$	Average velocity	[m s^{-1}]
u', v', w'	Velocity fluctuation	[m s^{-1}]
V_m	Molar volume	[m^3 mol^{-1}]
W	Weight percentage	[-]
α	Sticking coefficient	[-]
β_A	Impinging rate	[cm^{-2} s^{-1}]
γ	surface tension	[N m^{-1}]
σ	Surface tension	[N m^{-1}]
ρ	Density	[kg m^{-3}]
$\omega*$	Critical weight fraction	[-]

Symbol	Definition	Unit
$\Delta\mu$	Chemical potential change	[J mol^{-1}]
μ	Chemical potential	[J mol^{-1}]
$\bar{nu}$	Average volume per molecule inside the droplet	[cm^{-3}]
ξ	Concentration	[cm^{-3}]
λ	Correction factor	[-]
δ_i	Correction factor	[-]
η	Kolmogorov length scale	[m]
μ_{mole}	Ratio of molecular masses	[-]
μ	Dynamic viscosity	[N s m^{-2}]
ν	Kinematic viscosity	[m^2 s^{-1}]
ν_T	Eddy diffusivity	[m^2 s^{-1}]

List of Figures

List of Tables

1

Introduction

The Earth receives solar irradiance in the form of short wave radiation. Some of this sunlight is absorbed and part of it is radiated back to space. In addition, the Earth also emits long-wave radiation to space. The imbalance between total incoming and total outgoing radiation changes the Earth's global temperature until radiative equilibrium is restored. When the radiative imbalance is positive, meaning that there is more absorbed radiation than the combined reflected and emitted radiation, the temperature rises. As a response to surface warming, the outgoing long-wave radiation increases to restore the equilibrium. Natural and, primarily, anthropogenic processes have led to the trapping of radiation, e.g. due to increasing greenhouse gas (GHG) concentrations in the atmosphere. This has led to a positive radiative forcing (RF), i.e. positive net radiation imbalance. This imbalance has risen $0.79W/m^2$ between 2006 to 2018 resulting in increasing global temperatures. [1]

Geoengineering is the deliberate large-scale intervention in the Earth's natural systems, with the reduction of climate change induced risks as its main purpose. There has been a wide range of techniques proposed to achieve this, most of which can be divided in two categories. The first category is carbon geoengineering, which relates to the removal of GHG in the atmosphere in order to directly counter the growth of GHG concentrations and acidification of the oceans. The second category is solar geoengineering or solar radiation management (SRM), which is a form of geoengineering where part of the incoming sunlight is reflected back to space. [2]

This project aims at gaining knowledge within the field of SRM. A possible implementation technique for SRM which has been considered in numerical climate models is stratospheric aerosol injection (SAI) [3]. The injection of sulphate aerosols [4] or engineered solid aerosols like calcite [5] into the stratosphere, a relatively stable layer in the higher atmosphere at $20km$ altitude, would reduce the amount of short wave solar radiation reaching the surface and lower the radiative forcing, resulting in reduced global warming [6]. It is worth noting, however, that this would not offset the source of today's global warming which is the emission of GHGs. The use of engineered solid aerosols still has its unknowns and uncertainties, both in their impacts and their implementations [7]. This is less true for sulphate-based solutions. The injection of sulphate has its drawbacks, including ozone loss and the heating of the lower tropical stratosphere [5]. However, the properties and costs of sulphur are well known and sulphur is already present in the atmosphere either through volcanic or anthropogenic emissions. Furthermore, the side effects and radiative forcing of sulphates have been studied in more depth than engineered solid aerosols [8] [9] [10]. It is important to acknowledge that SRM, including all its various techniques, still entails numerous unknowns and uncertainties. These pertain not only to the physical processes but also to societal and political aspects such as governance and decision-making. While this study focuses on the physical aspects, it is crucial to recognize the broader context and emphasize that the physical component represents only a small fraction of the overall considerations.

1.1. State of the Art and Problem Statement

The size of aerosols affects their ability to scatter and absorb sunlight, smaller aerosols scatter more efficiently, while larger aerosols are more effective at absorbing and reflecting sunlight.Studies have shown that when sulphuric acid aerosols are injected, there is an optimal sulphate particle radius of approximately $0.125\mu m$ reached very early after injection for effective refraction of sunlight throughout the particle's residence time in the stratosphere [11]. These studies also showed that high rates of mixing and diffusivity the rate at which the exhaust plume behind the aircraft into which the direct H_2SO_4 is injected, grows through turbulent mixing with the background stratosphere, are beneficial for reaching the optimal radius after the early growth-stage [11]. There have been studies on whether precursor gasses like SO_2 or direct H_2SO_4 injection should be used. Those showed that direct H_2SO_4 injection is the most promising in terms of lower annual sulphur delivery rate, but only if high rates of mixing and diffusivity can be reached by injecting it behind an aircraft engine [12], [13].
The microphysical processes that take place during this phase affect aerosol size distribution downstream and are expected to have a large effect on possible SAI implementation scenarios. Therefore, improving the confidence in models describing this crucial aspect of SAI is essential to facilitate an informed discussion about SAI and its associated impacts and risks. Moreover, improvement of the initial conditions for global climate models should lead to a higher confidence in their results.

This project aims to get a better understanding of aerosol size distribution and the microphysical processes that govern them when injected behind a turbofan engine in the stratosphere. In particular, more knowledge is sought on the size distribution and concentrations of the H_2SO_4 aerosols, that determines the effectiveness of the method, by investigating if the optimal sulphate particle radius can actually be reached.

Explicit modelling of transient microphysical processes right after aerosol injection into a turbulent engine wake has not yet been done. The state of the art relies on models that assume the aerosols and their precursors are uniformly mixed throughout an exhaust plume's axial cross-section, and that the turbulence that grows the plume can be prescribed with simple empirical formulas. These are referred as box models throughout this report.

There has been research on aerosol dynamics in the near field of a propeller with a spatial variation for the SCoPEx stratospheric balloon experiment [14]. This research however, has orders of magnitude lower initial concentrations of H_2SO_4 and velocity and turbulent viscosity properties compared to an aircraft engine wake. The microphysical model for nucleation, condensation, and coagulation subroutines used in that research are based the Atmospheric and Environmental Research (AER) 2-D chemical transport model [15].

To summarise, the most important reference with comparable work are:

- Golja et al. [14]: Low-velocity and low-turbulence SCoPEx research that uses a 3D advective flowfield with AER 2-D microphysical mechanisms. Referred to as AER 3-D throughout this report.
- Pierce et al. [11]: Expanding lagrangian box model of the TwO-Moment Aerosol Sectional (TOMAS) microphysics model
- Benduhn et al. [13]: Box model for secondary aerosol formation using binary nucleation, brownian condensation and brownian and turbulent coagulation extended for plume dilulation

The aim in this research is to study the effects of introducing a more realistic non-uniform flow field. In this work a toolchain is set up with a one-way coupled computational fluid dynamics (CFD)-microphysics model where turbulent diffusivity and flow field parameters are calculated in a CFD solver using an axisymmetric method and are inserted in a second-order accurate advection-diffusion model coupled with the microphysical equations for nucleation, condensation and coagulation at every step. In order to effectively simulate the high temperature compressible flow behind an engine, it is necessary to utilise sophisticated CFD tools. These tools should also be capable of producing turbulence effects. If we adopt the Reynolds-Averaged Navier-Stokes (RANS) assumption, we can focus on an axisymmetric geometry, which helps reduce computational costs. To model the growth of the injected H_2SO_4 particles, we employ the AER 3-D software.

1.2. Research Objectives and Research Questions

This section itemises the research objectives and questions respectively.

The objective of this research is

”To achieve a better understanding of the processes that govern the formation, growth and final size distribution of H_2SO_4 aerosols in the first seconds after injection into an aircraft engine plume, by means of a sectional microphysics model in a flow field generated by CFD”

The main objective can be split up into four subobjectives:

- To obtain a model with appropriate microphysical equations to investigate the spatialevolution of the size distribution of aerosols in the early growth stage.
- To set up a CFD model of the engine wake of an aircraft using an axisymmetric 2D approach.
- To design a toolchain that can evolve an injection source in the microphysics model through the plume’s flow field generated by CFD
- To gain confidence in the model by comparing it to two state-of-the-art box model approaches [12], [13].

- To analyse the behaviour of aerosol formation and size distribution in a flow field with spatially varying conditions representative of an engine wake.

The main research question corresponding to the main research objective is

”Can a one-way coupled CFD-microphysics model be used to enhance our understanding of the formation, growth and final size distribution of H_2SO_4 aerosols during the early growth phase in an aircraft engine plume?”

To answer this question, the following subquestions are considered.

1. How does the quasi-one dimensional version of the AER 3-D model differ from the state-of-the-art box models?
    (a) How does the theory used in AER 3-D differ from that in the box models?
    (b) Which steps must be taken to compare the Lagrangian box models to the Eulerian AER 3-D model?
    (c) How do the outputs compare under the same conditions?
2. What is the effect of realistic engine conditions obtained from CFD on the prediction of aerosol growth using AER 3-D?
    (a) What influence do the microphysical mechanisms nucleation, condensation and coagulation have on the growth rate and size distribution of the aerosols?
    (b) What influence does the flow field with spatially varying conditions representative of an engine wake obtained from CFD have on the Q1D and axisymmetric cases ?
    (c) How do the turbulent diffusivity and thermodynamical flow state properties influence the aerosol size distribution in the axisymmetric case ?

1.3. Thesis Outline

The remainder of this report is structured as follows. The underlying theoretical framework and numerical implementation is given in Chapter 2. This theory will help understand the sectional aerosol model as outlined in Chapter 3, which describes the state-of-the-art approach to modelling the time evolution of aerosol size distribution in fluid flows in the field of SAI and geoengineering. Chapter 3 also explains the Reynolds-averaged Navier–Stokes (RANS) modelling of the engine wake. Thereafter, the coupling of these two elements is shown in the flowchart of the toolchain. In Chapter 4 the model is verified by comparing it to the box models. Then the results of the integration study are explained in Chapter 5, ending with Conclusion and Recommendations in Chapter 6.

2

Theoretical Framework and Numerical Implementation

This chapter first describes the equations governing the aerosol microphysics, accompanied by a comprehensive introduction to the variables involved. The second part of this chapter elaborates on the advection scheme to show where the flow field parameters are coupled. Finally this chapter considers aspects of turbulence modelling and eddy diffusivity in CFD.

2.1. Aerosol Microphysics

There are four microphysical processes that are of importance in modelling the behaviour of aerosols within the scope of this project: nucleation, coagulation, and condensation and evaporation.

Effective aerosol particles are droplets of aqueous H_2SO_4. Nucleation is the process where individual gaseous molecules of H_2SO_4 and H_2O combine to form clusters; the initial stage of aerosol particles. When these clusters collide with each other, they can merge into larger particles. This process is referred to as coagulation. In the formation of an aerosol cloud, these liquid particles can still be surrounded by gaseous H_2SO_4 and H_2O molecules that did not nucleate. These individual molecules can condense onto particles, referred to as condensation. These three processes result in aerosol growth. Aerosol particles can decrease in size through evaporation, where single molecules on the surface overcome the vapour pressure and are able to escape the liquid particle.

Figure 2.1 shows a schematic representation of timescales to show what microphysical mechanisms occur at each stage of plume development.

The main variables in the microphysical equations in this chapter are

- Flow variables: Velocity u_i, Pressure P
- Thermodynamic variables: Temperature T, Density ρ

- Aerosol variables: Size spectrum N_i, Radius r_i

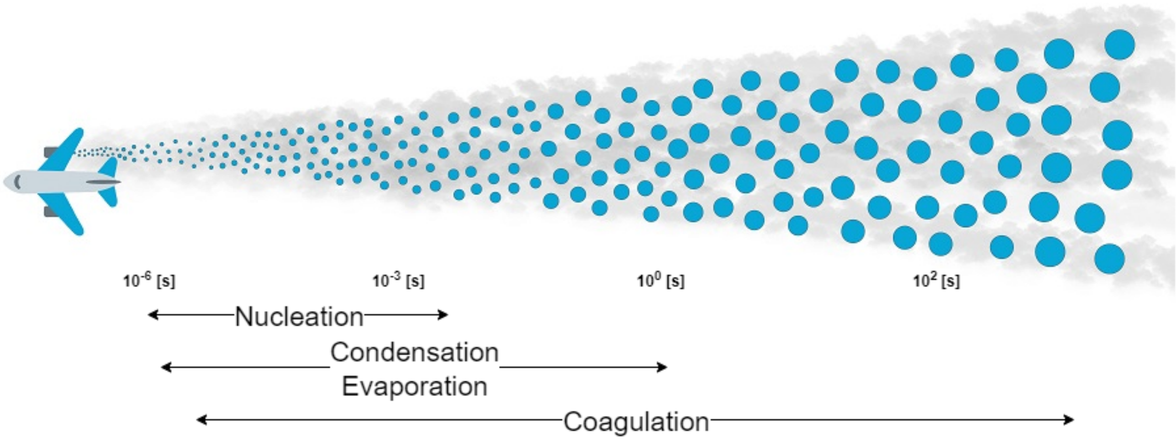

Figure 2.1: Domain of interest with a rough temporal overview to indicate which microphysical mechanisms are important in the wake of an engine following H_2SO_4 injection.

2.1.1. Size Categories

Aerosol particles can have different sizes, spanning multiple orders of magnitude from a few ångström to several microns. Particle size categories, or ”bins” are used to represent this range of sizes discretely. The smallest bin contains newly formed particles by nucleation, where particles formed by coagulation and condensation mechanisms take over in the larger size bins.

An approximate discrete equation in logarithmic space similar to that by Fuchs [16] is used for the analysis.

$$r_i = r_1 a^{b(i-1)} \tag{2.1}$$

With $a = 2$ and $b = 1/3$, this results in bins where the volume of one aerosol in bin i has twice the volume as one aerosol in bin $i - 1$.

2.1.2. Sulphate Aerosol Composition

The model calculates the composition of aerosols, specifically the weight percent of sulphuric acid, W, through an interactive process based on the ambient water vapour and temperature. This calculation follows the formula and tabulated values developed by Steele and Hamill [17]

$$\ln P^0 = A(W) \ln\left(\frac{T_e}{T}\right) + \frac{B(W)}{T} + C(W) + D(W)T \tag{2.2}$$

To determine the value of W that equalises the equilibrium vapour pressure, P^0, with the local value of water vapour partial pressure, we use tabulated values for A, B, C, and D, which are dependent on W and the equilibrium temperature, T_e, at 298.15 K. The composition of aerosols remains constant across all particle size bins. The mass M_i of H_2SO_4 bound within particles in bin i at grid point (I, J) is then calculated as

$$M_i(I,J) = \frac{3}{4}\pi r_i^3 D(I,J) * W(I,J) * N_i(I,J) \tag{2.3}$$

where D represents the bulk density of sulphuric aerosols and is also a tabulated value found in literature depending on aerosols composition and temperature [18].

2.1.3. Nucleation

There are three nucleation mechanisms that have to be considered when modelling sulphate aerosols in the stratosphere. The first, homogeneous heteromolecular nucleation, is described by homogeneous nucleation theory. Homogeneous indicates that the nucleation occurs in a uniform substance. Heteromolecular means that the nucleated particle can be composed of multiple types of molecules. This is typical for aerosol nucleation of sulphuric acid which produces $H_2SO_4 - H_2O$ clusters. Homogeneous, heteromolecular nucleation theory is applicable in regions of low temperature such as in the stratosphere, where at an altitude of $20km$ the average temperature is $218 - 223K$, and for high sulphuric acid or water vapour concentrations in the atmosphere. Yue and Deepack [19] state that relatively high concentrations of sulphuric acid are on the order of $10^3 - 10^8$ molecules cm^{-3}. These are comparable to concentrations resulting from the intrusion of volcanic clouds into the stratosphere.

The nucleation rate, J, used for homogeneous heteromolecular nucleation is defined as in Hamill [20]

$$J = 4\pi r^{*2}\beta_A N_B \exp\left(\frac{-\Delta G^*}{kT}\right) \tag{2.4}$$

With the parameters being

- r^* Cluster particle radius
- β_A Impinging rate of the gaseous H_2SO_4 molecules
- N_B Number density of water molecules
- ΔG^* Gibbs free energy saddle point value
- k Boltzmann constant
- T Temperature

The radius of the embryo, r^*, is defined as a function of the critical sulphuric acid weight fraction, ω^*, using

$$r^* = \frac{2\sigma(\omega^*)}{Y(\omega^*)} \tag{2.5}$$

where the microscopic surface tension of the embryo particle is denoted by σ. Parameter Y is defined as

$$Y = -\rho\left[\frac{\omega}{M_1}\Delta\mu_1 + \frac{1-\omega}{M_2}\Delta\mu_2\right] \tag{2.6}$$

When a changing from gas to liquid phase occurs, a change in chemical potential arises and is given by

$$\Delta\mu_i = \mu_i^l - \mu_i^g = -RT\ln\left(\frac{p_i}{p_i^0(T)}\right), i = 1,2 \tag{2.7}$$

p_i denotes the partial pressure of a gas-phase species, while p_i^0 represents the equilibrium vapour pressure of species i over a planar surface of the mixed solution at the specific temperature, T. R is the universal gas constant. The weight fraction itself is defined as

$$\omega = \frac{M_1 n_1}{M_1 n_1 + M_2 n_2} \tag{2.8}$$

where M_i is the molecular weight and the two-dimensional location of the saddle point is given by (n_1, n_2).

A relationship for the cluster radius as a function of the critical sulphuric acid weight fraction is given by Zhao [21]. This is necessary to compute the saddle point of the Gibbs free energy using

$$\Delta G^* = \frac{4}{3}\pi\sigma r^{*2} \tag{2.9}$$

Finally the impinging rate is given by

$$\beta_s = N_s \left(\frac{kT}{2\pi M_s}\right)^{1/2} \tag{2.10}$$

with M_s being the mass of one mole of H_2SO_4, $98.07848g$ and N_s is the number concentration of sulphuric acid. The gaseous sulphuric acid that is removed due to this nucleation mechanism is put in the bin size that is closest to the particle radius.

When kinetic nucleation occurs, parametrisation as described by Määttänen et al. [22] and Merikanto et al. [23] is used. This uses the temperature and relative humidity to calculate the kinetic threshold, C, which is the minimum required particle number density to be in the kinetic regime. The nucleation rate is described by

$$J_{\text{kin, neutral}} = \frac{C}{2}\sqrt{T}\left(N^{\text{total}}_{H_2SO_4}\right)^2 \tag{2.11}$$

with

$$C = \left(r_{H_2SO_4} + r_{\text{ref}}\right)^2 \sqrt{8\pi k \left(\frac{1}{m_{H_2SO_4}} + \frac{1}{m_{\text{ref}}}\right)} \tag{2.12}$$

where

$$r_{\text{ref}} = r_{H_2SO_4} = 0.3 \cdot 10^{-9}\ \text{m} \quad \text{and} \quad m_{\text{ref}} = m_{H_2SO_4} = 98.07 \cdot 1.661 \cdot 10^{-27}\ \text{kg} \tag{2.13}$$

The second nucleation mechanism is heterogeneous heteromolecular nucleation, where sulphuric acid droplets can be formed on pre-existing solid particles, like soot, in the engine plume. The theory for this process is that these solid particles adsorb water molecules onto their surface which then can attract sulphuric acid particles. The nucleation rate is then given by

$$J = 2\pi r^{*2}\beta_A N^{ads} \exp\left(\frac{-\Delta G^*}{kT}\right) \tag{2.14}$$

The new parameter here is N^{ads}, which represents the total number of water molecules that can be adsorbed on the surface of the solid particle per area and is defined by

$$N^{ads} \approx \beta \left[2.4 \times 10^{-16} \exp(\frac{10800}{\text{RT}})\right] \tag{2.15}$$

With R being the gas constant. The value 10800 is the heat of adsorption with unit $cal/mole$ and is considered reasonable for the solids that are found in the atmosphere. A further investigation into this number for use in an engine plume where other solid particles are present is still necessary.

The last nucleation mechanism that needs elaboration is ion nucleation. Ions, both positively and negatively charged, have a tendency to create small stable clusters of $2-5$ water molecules which H_2SO_4 molecules can strike and result in a stable solution droplet. The nucleation rate for this mechanism is defined by

$$J = 4\pi r^{*2}\beta_A \exp\left(-\delta\Delta G_i^*/kT\right) \tag{2.16}$$

with

$$\delta\Delta G_i^* = \Delta G_i\left(r^*\right) - \Delta G_i\left(r_1\right) \tag{2.17}$$

where the radii are the two saddle points in ΔG_i given by

$$\Delta G_i = \Delta G_{\text{homog}} + \frac{q^2}{2}\left(1-\frac{1}{\varepsilon}\right)\left(\frac{1}{r}-\frac{1}{r_0}\right) \tag{2.18}$$

Where the latter addition is the electrostatic free energy contribution of the ion.

Parameterization has been done by Vehkamäki et al. [24] for the homogeneous nucleations rates and Määttänen et al. [22] for further developed homogeneous rates and ion-induced rates. Both parametrizations are valid in higher temperature ranges and H_2SO_4 concentrations, up to $400K$ and $10^{16}cm^{-3}$ for ion-induced nucleation and $305K$ and $10^{11}cm^{-3}$ for homogeneous nucleation. Realistic engine plumes will have higher temperatures and relevant SAI scenarios might inject higher concentrations of sulphuric acid. As there are no other models for nucleation rates available at these temperatures, however, it will be assumed that these models still apply.

2.1.4. Condensation and Evaporation

Condensation of sulphuric acid and water vapour on pre-existing $H_2SO_4 - H_2O$ droplets is the predominant mechanism that causes gas-phase conversion under normal stratospheric conditions.

Here it is considered that the condensation process to be a molecular diffusion process described by the rate of change of the particle radii due to this heteromolecular condensation or evaporation as [20]

$$\frac{dr}{dt} = \frac{\bar{\nu} D\left(P_s - P_s^0\right)/(kT)}{r\chi\left(1+\lambda K_n\right)} \tag{2.19}$$

With the parameters being

- $\bar{\nu}$ Average volume per molecule inside the droplet
- D Diffusion coefficient
- χ Concentration of H_2SO_4 inside the droplet
- λ Correction factor, in function of Knudsen number and sticking coefficient α.

- K_n Knudsen number
- P_s Ambient sulphuric acid vapour pressure
- P_s^0 Partial vapour pressure over the droplet surface.

The term $(P_s - P_s^0)$ expresses if either condensation or evaporation occurs. When the term is larger than zero, aerosol radii increase by condensation. When the term is smaller than zero, evaporation is assumed.

The correction factor is described as

$$\lambda = \frac{1.333 + 0.71\text{Kn}^{-1}}{1 + \text{Kn}^{-1}} + \frac{4(1-\alpha)}{3\alpha} \tag{2.20}$$

with α being the sticking coefficient, which can be assumed to be unity in this case [25], essentialy removing the second term. The diffusion coefficient is given as [26]

$$D = \frac{1}{3}\left(\frac{8kT}{\pi M_S}\right)^{\frac{1}{2}} l_{\text{eff}} \tag{2.21}$$

with M_s being the mass of one mole of H_2SO_4, $98.07848g$ and l_{eff} the effective mean free path of molecules.

An effect to consider when modelling condensation and evaporation is the Kelvin effect. It refers to the reduction in saturation vapour pressure over a curved liquid surface compared to a flat surface. When a droplet is in equilibrium with its surrounding vapour, its curvature causes an increase in the internal pressure, which lowers the saturation vapour pressure inside the droplet. This lower saturation vapour pressure leads to a decrease in the evaporation rate of the droplet. As a result, smaller droplets, with higher curvature and therefore greater internal pressure, have a reduced tendency to evaporate compared to larger droplets, providing them with a thermodynamic advantage for survival and growth in a supersaturated environment. The ratio of the equilibrium vapour pressure over a curved surface to a flat surface is given by the Kelvin equation [5]

$$\frac{P}{P_0} = \exp\left(\frac{2\gamma V_m}{rRT}\right) \tag{2.22}$$

with the surface tension γ and V_m being the molar volume.

2.1.5. Coagulation

When two particles or droplets collide, they can form a new aerosol particle or droplet that has an increased size, this is called coagulation. This results in a decreased total number of particles with an increased diameter.

There are two types of coagulation that need to be considered. The first is coagulation due to Brownian motion, which is a thermal process. The second is coagulation due to external forces. Examples of the latter include electrical or hydrodynamic forces. In the wake of an engine however, turbulence provides the most important external force. Turbulence affects the collision properties of aerosols via four different mechanisms [27]:

- Acceleration effect: Increased particle velocities and more random velocity directions

- Shear effect: The shear forces in the flow field resulting from velocity gradients cause particles to collide even when they have the same initial inertia. [28]
- Accumulation effect: When the response time of particles (a function of the particle Stokes number) is on the order of the smallest scales in a turbulent flow, namely the Kolmogorov microscale, the coagulation rates are increased as the local concentrations build up. [29]
- Hydrodynamic effect: Collision efficiency is larger in a turbulent flow. Both the magnitude and orientation of droplet-droplet relative motion and the local distribution of the particles in the flow-field is altered by turbulent characteristics. [30] [31]

The standard treatment of aerosol size redistribution due to coagulation used is given by Fuchs [16]

$$\frac{\partial n_i}{\partial t} = -n_i \sum_{j\neq i} K_{ij} n_j - \frac{1}{2} K_{ii} n_i^2 + \frac{1}{2} K_{i-1,i-1} n_{i-1}^2 + n_i \sum_{j<i} (1 - \frac{V_j}{V_i}) K_{ij} n_j + \sum_{j<i-1} \frac{V_j}{V_{i-1}} K_{i-1,j} n_{i-1} n_j \tag{2.23}$$

with the parameters being

- n_i Number of particles in bin i
- K_{ij} Coagulation kernel between particles with bin size i, j
- V_j/V_i Volume ratio added to the larger size bin

The coagulation kernels are computed by the method in [32]. To determine the frequency of collisions per unit volume between particles in size bin i and size bin j, the collision is assumed to be a two-body collision mechanism due to Brownian diffusion. The coagulation kernels that are used from Fuchs et al. [16] are

$$K(r_i, r_j) = K_{ij} = 4\pi r_{ij} D_{ij} \left(\frac{r_{ij}}{r_{ij} + \delta_{ij}} + \frac{4D_{ij}}{G_{ij} r_{ij}} \right)^{-1} \tag{2.24}$$

where

$$\left.\begin{aligned} r_{ij} &= r_i + r_j \\ D_{ij} &= D_i + D_j \\ G_{ij} &= \left(G_i^2 + G_j^2\right)^{1/2} \\ \delta_{ij} &= \left(\delta_i^2 + \delta_j^2\right)^{1/2} \end{aligned}\right\} \tag{2.25}$$

r_i and r_j are the radii in the corresponding size bins, δ_i and δ_j are the correction factors, and G represent the average kinetic velocity. D_i and D_j are the diffusion coefficients that are calculated using Einstein's relation of $D = kTB$, with k being the Boltzmann constant of $1.38 \cdot 10^{-23} m^2 kg s^{-2} K^{-1}$, T being the absolute temperature and B the mobility within the fluid given by

$$B = \frac{1}{6\pi \eta_m r} \left[1 + 1.246 K_n + 0.42 K_n \exp\left(-\frac{0.87}{K_n} \right) \right] \tag{2.26}$$

Here μ_m represents the viscosity of the air and K_n is the Knudsen number which is defined by

$$K_n = l_{eff}/r \tag{2.27}$$

with the effective mean free path of molecules being

$$l_{eff} = (\pi n d^2 \mu_{mole}^{0.5})^{-1} \tag{2.28}$$

Here n is the air molecules number density, d is the average diameter of an air molecule and the considered coagulating particle, and μ_{mole} is a ratio of molecular masses of air and the particle defined by $\mu = M_{air}/(M_{air} + M_{aerosol})$. Air molecules that are present in the atmosphere are mainly Nitrogen (N_2) and Oxygen (O_2).

The correction factor δ_i is made up of components defined by

$$\delta_i = \frac{1}{6rl_b}\left[(2r_i + l_b)^3 - \left(4r_i^2 + l_b^2\right)^{3/2}\right] - 2r_i \tag{2.29}$$

with l_b defined as

$$l_b = (8D_i)/(\pi G_i) \tag{2.30}$$

Finally, G_i represents the average kinetic velocity of a particle suspended in the air and is defined by

$$G_i = \left(\frac{8KT}{\pi m_i}\right)^{1/2} \tag{2.31}$$

Here m_i is the mass of the particle in bin size i.

The above derivation of the coagulation kernels is applicable to still air or in models where no turbulence affects the coagulation of aerosols. Sundaram and Collins [33] derived a collision kernel equation in a turbulent gas and Zhou et al. [34] studied the turbulent collision kernel using direct numerical simulations to parametrize the kernels accordingly.

Turbulent collision kernels are governed by

$$K_{t,0}\left(r_1, r_2\right) = \Gamma_0 \frac{\left\langle\left|w_r\left(r_1, r_2\right)\right|\right\rangle}{\left\langle\left|w_{r,\text{ shear}}\left(r_1, r_2\right)\right|\right\rangle} g_{12}(R) \tag{2.32}$$

With $R = r_1 + r_2$ being the collision radius and the collision kernel for zero-inertia being

$$\Gamma_0 = \sqrt{\frac{8\pi}{15}} R^3 \frac{v_k}{\eta} \tag{2.33}$$

It is in this equation that the Kolmogorov velocity scale is used as $\nu_k = (\nu\epsilon)^{1/4}$, with ν being the kinematic viscosity of air ($1.81 \cdot 10^{-5} m^2 s^{-1}$ at $288K$) and ϵ being the average rate of dissipation of TKE per unit mass. The Kolmogorov length scale is defined as $\eta = (\nu^3/\epsilon)^{1/4}$. The absolute value of the radial relative velocity of the corresponding particles is given by $\left\langle\left|w_r\left(r_1, r_2\right)\right|\right\rangle$, this is the relative velocity between two particles on the line intersecting both particles. The final parameter in this equation is the factor g_{12} in function of the collision radius, R. This is the bidisperse radial distribution function at contact and regards the accumulation effect as described in the beginning of this subsection.

2.2. Lax-Wendroff Advection scheme

When transitioning from box models to Eulerian 3-D models, the inclusion of an advection scheme becomes necessary to represent transport processes. In box models, the transport of substances is simplified and assumes instantaneous mixing throughout the plume area. However, in Eulerian 3D models, the domain is discretised into grid cells, and the movement of aerosols needs to be accurately accounted for as they are advected through the aircraft plume.

The Lax-Wendroff advection scheme is a numerical method used to solve advection-diffusion equations. When combined with a flux limiter, such as the Superbee flux limiter, it provides second-order accuracy. An example grid with all points and parameters needed for this is given in Figure 2.2.

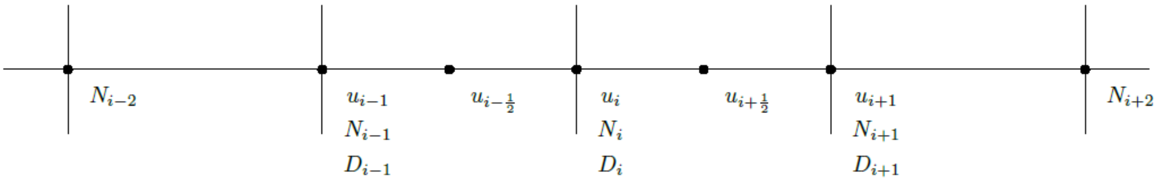

Figure 2.2: Gridpoints and parameters for the Lax-Wendroff advection scheme with a Superbe flux limiter

For readability, only the x-direction component is considered in this section. The equations for the Lax-Wendroff advection scheme with a Superbee flux limiter, can be expressed as follows:

$$N_i^{n+1} = N_i - \frac{dt}{dx} \cdot u_{i-\frac{1}{2}} N_{i-\frac{1}{2}} - u_{i+\frac{1}{2}} N_{i+\frac{1}{2}} + \frac{d^2 t}{dx^2} \cdot diff_x \tag{2.34}$$

$$N_{i+\frac{1}{2}} = (N_i + \frac{1}{2}(N_{i+1} - N_i)\phi_{sb})\chi_{i-\frac{1}{2}} + (N_{i-1} - \frac{1}{2}(N_{i+1} - N_i)\phi_{sb})\chi_{i+\frac{1}{2}} \tag{2.35}$$

χ is 0 or 1 depending whether flow flowing into the cell or out of the cell. The Superbee limiter is defined as

$$\phi_{sb}(r) = \text{max}[0, \text{min}(2r, 1), \text{min}(r, 2)]; \quad \lim_{r \to \infty} \phi_{sb}(r) = 2. \tag{2.36}$$

and r is the ratio of consecutive gradients defined as

$$r_i = \frac{u_i - u_{i-1}}{u_{i+1} - u_i} \tag{2.37}$$

The diffusion in x dimension is defined as follows

$$diff_x = \frac{k_{i-1} - k_{i+1}}{2} \frac{N_{i-1} - N_{i-1}}{2} + k_i(N_{i-1} + N_{i+1} - 2N_i) \tag{2.38}$$

It shows the dependence of the diffusion, D, that will be the parameter to couple the turbulent diffusivity to later in this report.

2.3. Plume Computations and Turbulent Diffusivity in CFD

This chapter describes the possible CFD methods and a short introduction to turbulent diffusivity in the chosen simulation method of RANS.

2.3.1. Simulation Methods

This sub-chapter will briefly introduce flow-field variables and CFD methods. For the CFD method that is chosen in this research, the effects of turbulence are modelled. The reasoning behind the chosen turbulence model is provided.

Diffusion in laminar flow is governed by molecular motion. For turbulent flow however, there is also diffusion due to eddy motion. The latter can be modelled by adding an eddy viscosity coefficient to the diffusion coefficient in the momentum and energy equations. The mechanism of eddy viscosity lacks actual physical meaning.

The terms 'diffusivity' and 'viscosity' are often used interchangeably in fluid dynamics literature as the kinematic viscosity is sometimes called momentum diffusivity. For this project the following terms are defined with their respective SI units.

Parameter	Symbol	SI unit	Other units
Dynamic viscosity	μ	$N \cdot s/m^2$	$Pa \cdot s, kg \cdot m^{-1} \cdot s^{-1}$
Kinematic viscosity Momentum diffusivity	$\nu = \frac{\mu}{\rho}$	m^2/s	
Eddy viscosity coefficient Eddy diffusivity	ν_T or sometimes K	m^2/s	

Table 2.1: Viscosity variables

As can be seen, the kinematic viscosity is defined as the dynamic viscosity divided by the density of the fluid. The kinematic viscosity therefore has only to do with the flow and not with the fluid.

The three main CFD simulation methods are Direct Numerical Simulation (DNS), Large Eddy Simulation (LES) and Reynolds' Averaged Navier-Stokes (RANS). In DNS, all turbulent structures are accurately resolved in space and in time, which requires a very fine grid and time steps, and a cost scaling with approximately Re^3. This method is too computationally intensive for this application. It is mostly used for simple flows in research and academia, where Reynolds numbers are relatively low [35]. This is not the case in this project, for which Re is on the order of $1e^6$.

The second method, LES, attempts to resolve all gradients of the mean flow and the most energetic (largest) turbulent structures in space and time. That is, the flow is decomposed in resolved and unresolved scales. The effect of the unresolved scales (sub-grid scale (SGS)) on the resolved scales is modelled. This method is still computationally expensive.

The third method is RANS, where only gradients and structures of the mean flow are resolved.

Turbulent structures are not resolved but accounted for using a model for the Reynolds stress tensor. Steady RANS was used in this project, as it has the lowest complexity and computational time. The time averaged solution of a turbulent plume when we assume no swirl, referring to the rotational motion of fluid particles around the central axis of a flow, is axisymmetric. Therefore there is no need to consider anything more than axisymmetric when using RANS.

2.3.2. RANS and Eddy Viscosity Models

In order to illustrate Reynolds Averaging, examine the incompressible Navier-Stokes (N-S) equations in the absence of any external body forces.

$$\begin{gathered}\nabla \cdot \vec{V} = 0 \\ \rho \left[\frac{\partial \vec{V}}{\partial t} + \vec{V} \cdot \nabla \vec{V} \right] = -\nabla p + \mu \nabla^2 \vec{V}\end{gathered} \tag{2.39}$$

The velocity vector is defined as $\vec{V} = [u, v, w]^\intercal$. The decomposition of a velocity is described as $\bar{u}+u'$. Where the barred parameter denotes the average and the primed parameter are the velocity fluctuations. By replacing the decomposed velocity components, the continuity equation can be expressed as follows

$$\nabla \cdot \left[(\bar{u} + u')\,\hat{\imath} + (\bar{v} + v')\,\hat{\jmath} + (\bar{w} + w')\,\hat{k} \right] = 0 \tag{2.40}$$

After performing time averaging, it becomes evident that the average of the fluctuating velocities becomes zero, resulting in

$$\overline{\nabla \cdot \vec{V}} = \nabla \cdot \left(\bar{u}\hat{\imath} + \bar{v}\hat{\jmath} + \bar{w}\hat{k} \right) = 0 \tag{2.41}$$

here the mean velocity vector $\overline{\vec{V}}$ is defined as $\bar{u}\hat{\imath} + \bar{v}\hat{\jmath} + \bar{w}\hat{k}$, the RANS continuity equation has the identical from as the original N-S continuity equation. When applying this to the momentum equations, the following RANS equation is obtained

$$\rho \left[\frac{\partial \vec{V}}{\partial t} + \vec{V} \cdot \nabla \vec{V} \right] + \rho \frac{\partial}{\partial x_j} \left(\overline{u_i' u_j'} \right) = -\nabla \bar{p} + \mu \nabla^2 \vec{V} \tag{2.42}$$

This can be re-arranged to

$$\rho \left[\frac{\partial \overrightarrow{\vec{V}}}{\partial t} + \overrightarrow{\vec{V}} \cdot \nabla \overrightarrow{\vec{V}} \right] = -\nabla \bar{p} + \nabla \cdot \tau_{ij} \tag{2.43}$$

where the Reynold's stress tensor is defined as

$$\tau_{ij} = \mu \left(\frac{\partial \bar{u}_i}{\partial x_j} + \frac{\partial \bar{u}_j}{\partial x_i} \right) - \rho \overline{u_i' u_j'} \tag{2.44}$$

RANS requires modelling of the Reynolds stresses. Equation 2.43 is numerically solved but a model must be posed for the Reynolds stresses, $\rho\overline{u_i' u_j'}$, in the second term of Eq. 2.44. The turbulence models that are often used are Eddy Viscosity Models (EVM) or Reynolds Stress Models (RSM). There have been multiple studies that showed that the EVM method using the Shear Stress Transport (SST) model by Menter and Wilcox [36] [37] shows the best results for turbulent free jet flow [38], so this will be discussed below. This model is also available within ANSYS, the commercial CFD solver that will be used here, explained more extensively in the methodology part of this report.

This SST model solves the Navier-Stokes' closure problem with a two-equation model using turbulent kinetic energy and dissipation of the turbulent energy and combines the best of both worlds from the $k-\epsilon$ and $k-\omega$ models. At the inlet conditions, the $k-\omega$ model is used for its robustness in wall vicinity and high pressure gradients, where-after the $k-\epsilon$ model is employed for better external aerodynamics.

The transport equation for turbulent kinetic energy in the $k-\epsilon$ model is described by

$$\frac{\partial k}{\partial t} + \langle u_j \rangle \frac{\partial k}{\partial x_j} = \tau_{ij} \frac{\partial \langle u_i \rangle}{\partial x_j} + \frac{\partial}{\partial x_j}\left(\left[\frac{1}{\mathrm{Re}} + \frac{v_t}{\mathrm{Pr}_k}\right]\frac{\partial k}{\partial x_j}\right) - C_D \frac{k^{3/2}}{l_m} \tag{2.45}$$

with the mixing length defined as

$$l_m = C_D \frac{k^{3/2}}{\epsilon} \tag{2.46}$$

while the additional transport equation for the turbulent dissipation is

$$\frac{\partial \varepsilon}{\partial t} + \langle u_j \rangle \frac{\partial \varepsilon}{\partial x_j} = C_{\varepsilon 1} \frac{\varepsilon}{k} \tau_{ij} \frac{\partial \langle u_i \rangle}{\partial x_j} + \frac{\partial}{\partial x_j}\left(\left[\frac{1}{\mathrm{Re}} + \frac{v_t}{\mathrm{Pr}_\varepsilon}\right]\frac{\partial \varepsilon}{\partial x_j}\right) - C_{\varepsilon 2} \frac{\varepsilon}{k} \varepsilon \tag{2.47}$$

The eddy viscosity is defined as

$$\nu_T = C_D \frac{k^2}{\epsilon} \tag{2.48}$$

and the Reynolds' stress tensor as

$$\tau_{ij} = 2 v_T S_{ij} - \frac{2}{3} \delta_{ij} k \tag{2.49}$$

with

$$\begin{aligned} \delta_{ij} &= \begin{cases} 1 & \text{, if } i = j \\ 0 & \text{, if } i \neq j \end{cases} \\ S_{ij} &= \tfrac{1}{2}\left(\tfrac{\partial \langle u_i \rangle}{\partial x_j} + \tfrac{\partial \langle u_j \rangle}{\partial x_i}\right) - \tfrac{1}{3}\delta_{ij}\tfrac{\partial \langle u_k \rangle}{\partial x_k} \end{aligned} \tag{2.50}$$

The other constants in the transport equation are $C_D = 0.09, Pr_k = 1, Pr_\epsilon = 1.3, C_{\epsilon 1} = 1.44, C_{\epsilon 1} = 1.92$. These coefficients are obtained by calculating simple flows where k and ϵ cancel each other.

3

Methodology and Toolchain

This chapter explains the toolchain developed for this research. The flowchart in Figure 3.1 shows an overview of the routines used. First the GSP Engine Model is described in Section 3.1, the model uses the engine parameters that are described by Janssens et al. as input and produces engine exit velocities and temperature as output. The engine exit parameters serve as inlet boundary conditions for the ANSYS Fluent RANS calculations in Section 3.2, this section also explains the geometry, domain and mesh sizing. The output of the RANS calculations is an axisymmetric 2-D field of flow velocity, temperature and turbulent viscosity. This flow field is transformed in MATLAB to achieve a full 3-D flow field and is explained in Section 3.3. This 3-D flow field can be inserted in the AER 3-D model, explained in Section 3.4, where the temperature field is used in the microphysical routines. As described was Section 2.1.2, the sulphate aerosol composition and microphysical routines are governed by temperature. The velocity and turbulent viscosity fields are inputs for the Lax-Wendroff advection transport scheme as described in Section 2.2, which showed how turbulent viscosity is used for the diffusion term of the advection scheme.

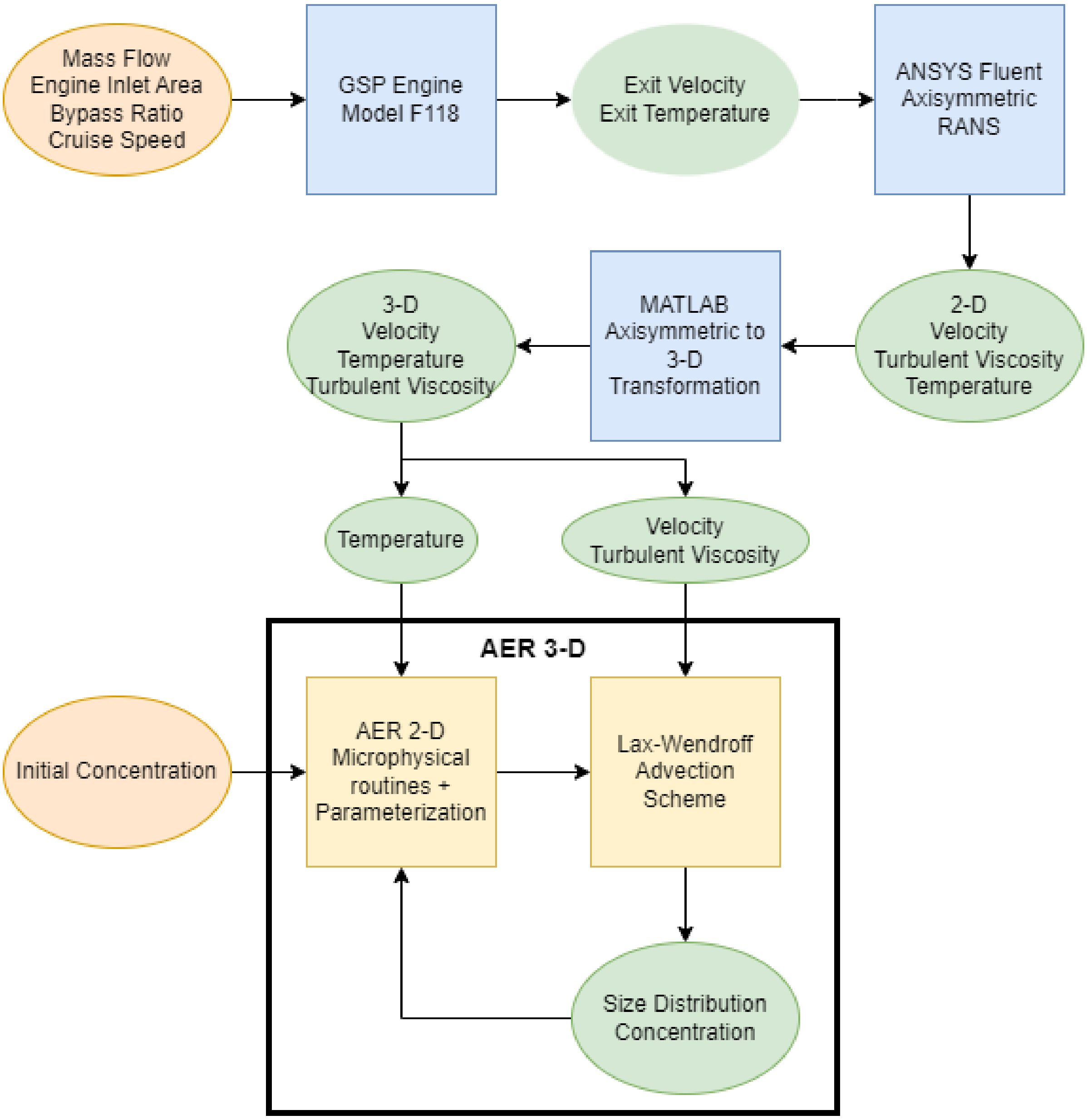

Figure 3.1: Toolchain flow chart including all inputs and outputs and corresponding modules that use these.

3.1. GSP Engine model

The output of the engine model is used for the boundary inlet condition for the RANS calculations. The figure below shows the schematic overview of a low by-pass engine that can be used at high altitudes for SAI based on Janssens et al. [12]. This engine was based on an F118 but has a larger diameter and a bypass ratio of 7.5, other parameters from the Janssens et al. study is found in Table 3.1.

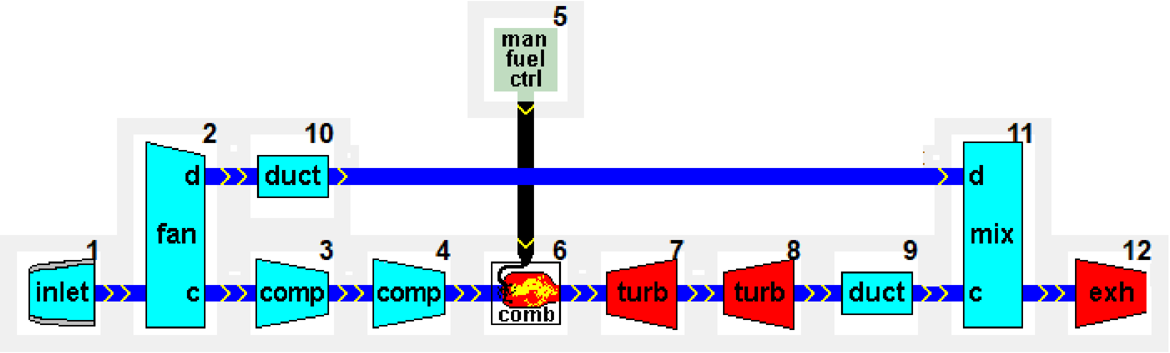

Figure 3.2: GSP Engine model of the adjusted F118 according to the study by Janssens et al. [12]

Mass flow	35.240	kg/s
Engine inlet area	9.62	
Cruise speed V_c	210	m/s
Bypass Ratio	7.5	-

Table 3.1: Engine and cruise speed properties according to the study by Janssens et al. [12]

The velocity at the outlet of point 12 was found to be $450m/s$ and an exit temperature of $570K$. These values were used as inlet boundary conditions in the RANS calculations.

3.2. RANS Calculations in ANSYS

This section describes the modelling and assumptions of the ANSYS Fluent RANS calculations of the engine wake. Its output velocity and eddy viscosity fields were then used for the advection scheme to advect the particles in the engine wake.

3.2.1. Geometry, domain and mesh sizing

An initial axisymmetric domain of $18m$ in radial direction, r, and $200m$ in axial direction, x, was used. As computational time is a limiting factor in this research, the minimum recommended width in radial direction was chosen which is five times the diameter of the engine.

The inlet boundary condition for the axial velocity in ms^{-1} is described as

$$u = \begin{cases} 450, & \text{if } r < 1.75 \\ 450 - [1 - \cos(\frac{\pi(r-1.75)}{0.25}\frac{450-210}{2}), & \text{if } 1.75 \leq y \leq 2.00 \\ 210, & \text{if } r > 2.00 \end{cases}$$

As shown in Figure 3.3 below, to ensure stability of the shear layer at the exit of the jet, a width of $25cm$ was used. A benefit of this is that it can also mimic the lower velocities of the bypass flow of the engine. The maximum velocity was taken as $450m/s$ and the free stream velocity is the assumed cruise speed of the aircraft at $210m/s$. All these velocities are initially only in the axial-component of the flow direction. The ANSYS Fluent standard turbulence intensity of 5% was not enough to assure stability and is increased to 10%, this is also in the order of turbulence intensity of engine wakes. As this is an axisymmetric 2-D space calculation, an axis of symmetry in the center of the wake is taken as boundary condition. For the outflow boundary condition, a pressure outlet was used with the operational atmospheric pressure at $20km$ height.

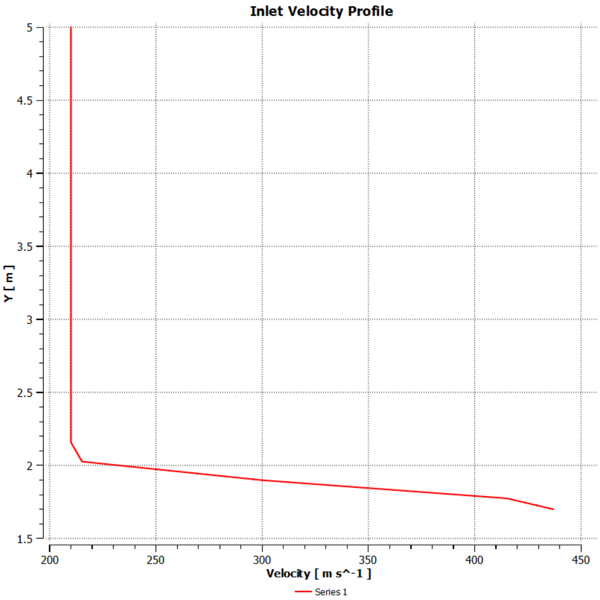

Figure 3.3: Velocity input profile for boundary layer

Figure 3.4 show the complete meshed domain. The left and top of the domain are the velocity inlets, the right side is the pressure outlet and the axis of symmetry is found at the bottom. The inlet is divided in 2 part as shown in Figure 3.5, where part 1 represents the free-stream inlet and part 2 of the inlet represents the engine outlet.

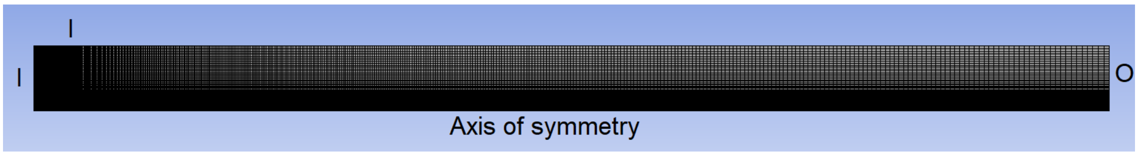

Figure 3.4: Full domain denoting the boundary conditions

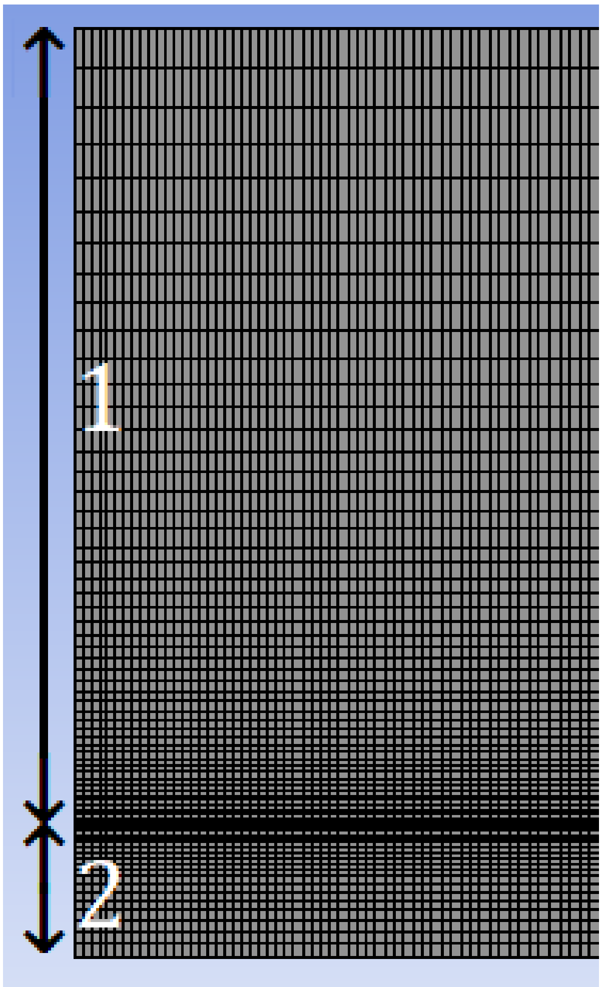

Figure 3.5: Inlet boundary conditions where 1 represents the free-stream inlet and 2 inlet condition that is the engine outlet

The domain was meshed in radial and axial direction with edge sizing using number of divisions (NOD). The number of cells in axial direction, n_x, had 1000 divisions whereas the number of cells in radial direction, n_r, had 25 divisions in the engine outlet and 50 in the free-stream area. As the free-stream width of the domain is 10 times larger than the engine outlet, this results in the engine outlet mesh to be much finer than the free-stream area above it even though it has less divisions. Both mesh edges had a bias factor of 10, which is a parameter that implies the growth rate of the elements, where the size of the cell mesh increases away from the engine outlet. Figure 3.6 below shows the mesh sizing.

Parameter	Value
C_μ	0.09
$C_{1\epsilon}$	1.44
$C_{2\epsilon}$	1.92
TKE Prandtl Number	1
TDR Prandtl Number	1.3
Energy Prandtl Number	0.85
Wall Prandtl Number	0.85

Table 3.2: Model constants for the $k - \epsilon$ turbulence model used in ANSYS Fluent.

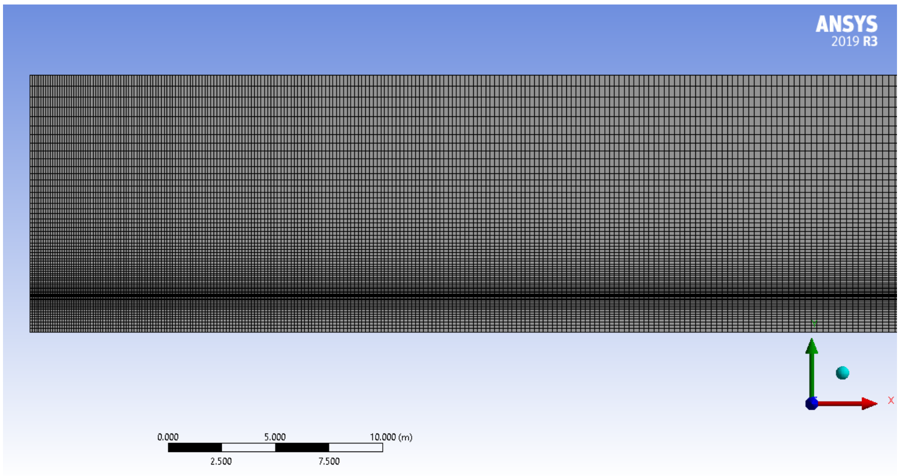

Figure 3.6: Fine mesh ANSYS Fluent, with $n_x = 1000$ and $n_r = 75$

3.2.2. RANS Set-up and turbulence modelling

The turbulence modelling used is the standard SST $k - \epsilon$ turbulence model with standard ANSYS values, Table 3.2, for α and β model constants as described in Section 2.

The simulation was run using 5000 iterations with a time-step of $1e^{-5}[s]$. The residuals are shown below. These show a large unsteadiness but it can be assumed that an absolute residual of $1e - 04$ was achieved, they will not have a large influence on the analysis of aerosol behaviour.

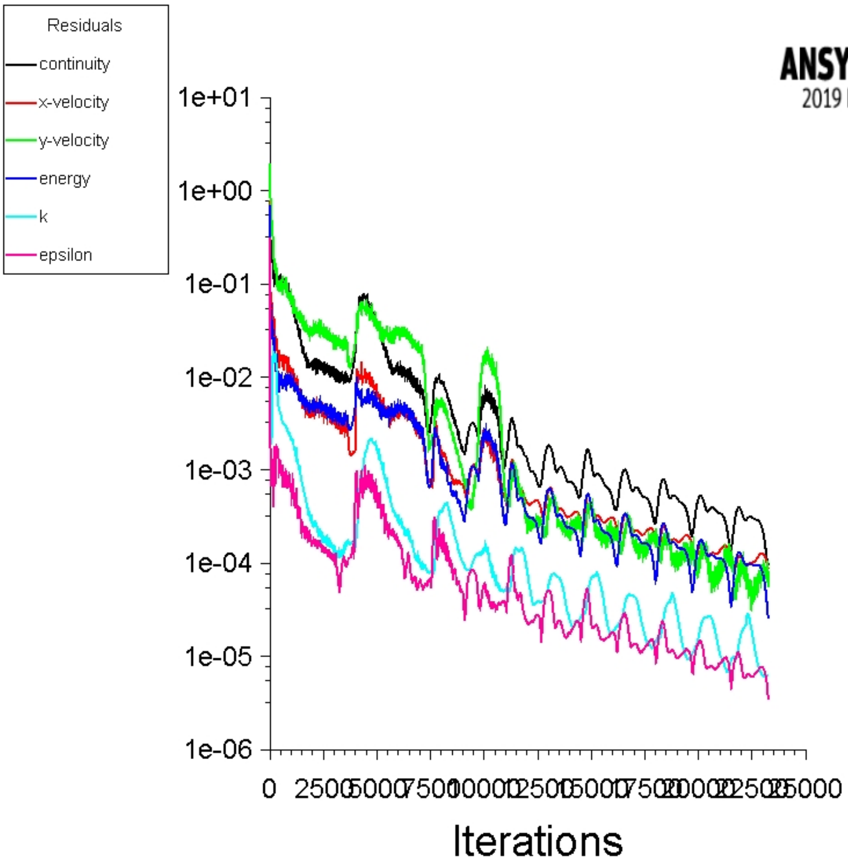

Figure 3.7: Residuals of the fine solution

3.2.3. Mesh convergence study

To ensure that the solution is independent of the grid resolution, a mesh convergence study was done. The solutions below show the turbulent viscosity for the reference case and for a mesh with half the number of divisions in the radial direction. The maximum turbulent viscosity in the flow-field is 0.58 and 0.591 respectively. This results in a difference of 1.8%. As a different choice of turbulence model can result in a the difference in maximum turbulent viscosity that can range from a few percent to several orders of magnitude, depending on the complexity of the flow and the accuracy of the turbulence model, this is relatively low compared to that. The main visual difference is the width of the shear layer seen in Figure 3.8 and 3.9, which has a better resolution in the study where the free stream is divided by 50.

The same can be seen in Figure 3.10 and 3.11 which shows a maximum temperature difference of only 0.2%. The temperature gradients are more prominent at the engine outlet. Here the mesh is well defined, however so that there are no noteworthy visual differences.

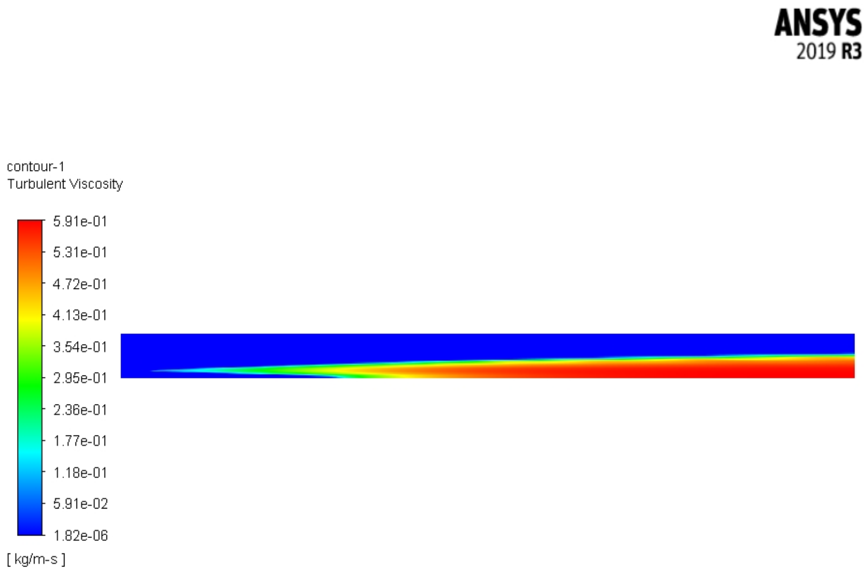

Figure 3.8: Turbulent viscosity solution for number of divisions in the engine outlet = 10 and free stream = 25

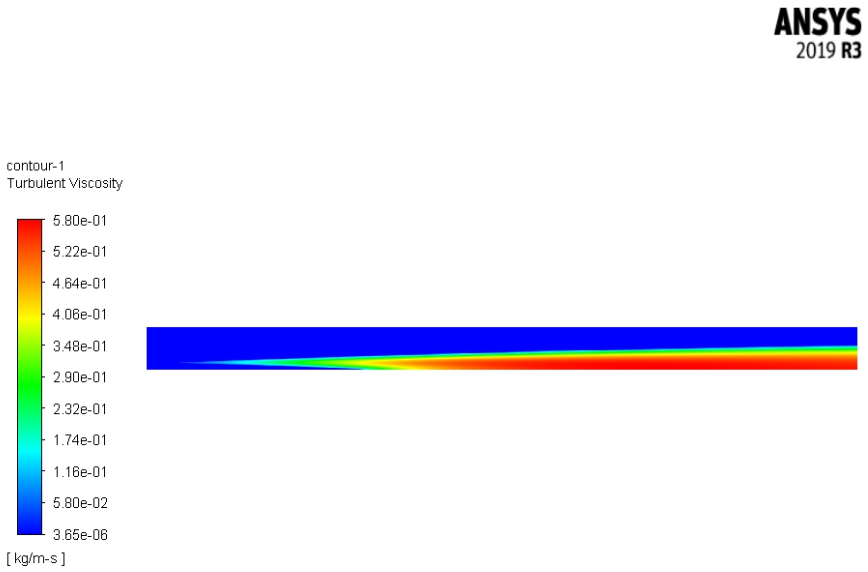

Figure 3.9: Turbulent viscosity solution for number of divisions in the engine outlet = 20 and free stream = 50

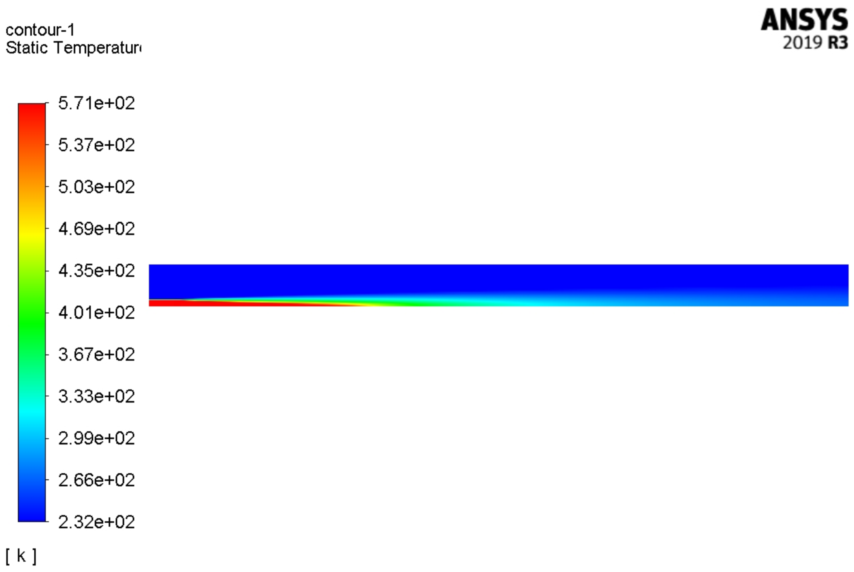

Figure 3.10: Static temperature solution for number of divisions in the engine outlet = 10 and free stream = 25

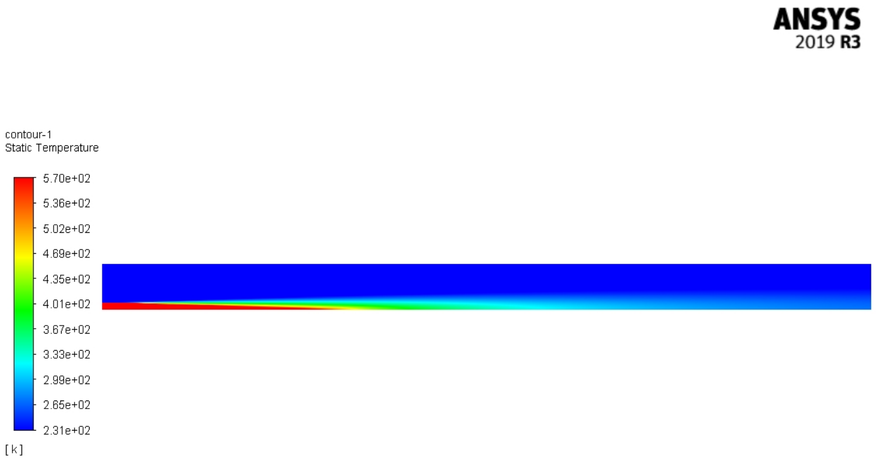

Figure 3.11: Static temperature solution for number of divisions in the engine outlet = 20 and free stream = 50

3.3. Transformation from an axisymmetric to a 3-D coordinate system

Once the solution on the fine mesh are computed, the built-in interpolation function in ANSYS was used to interpolate the solutions from the fine mesh to a coarser mesh with cell dimensions of $1 \times 1m$ as shown in Figure 3.12. This dimension was used as input for the AER 3-D model.

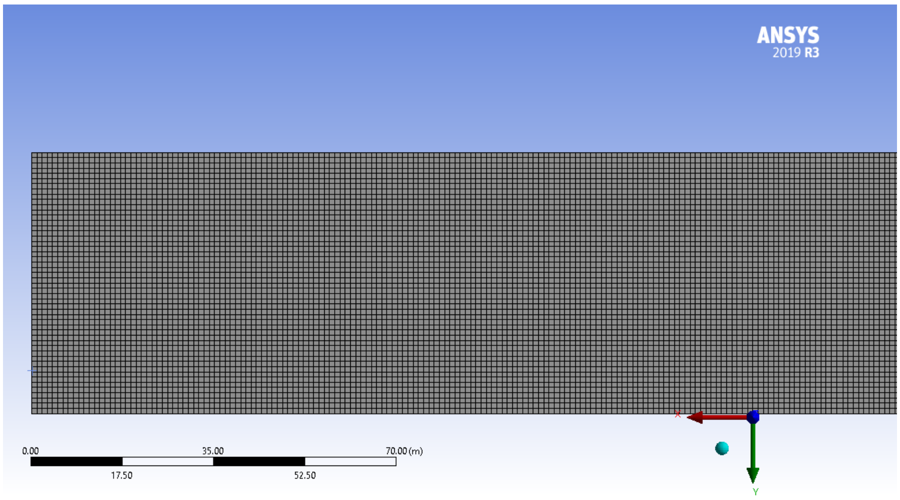

Figure 3.12: Microphysical mesh that is used in the AER 3-D model.

The results of the coarse axisymmetric 2-D RANS calculations were then transformed into a 3-D mesh in order to provide input compatible with AER. A visualisation of this transformation is shown below.

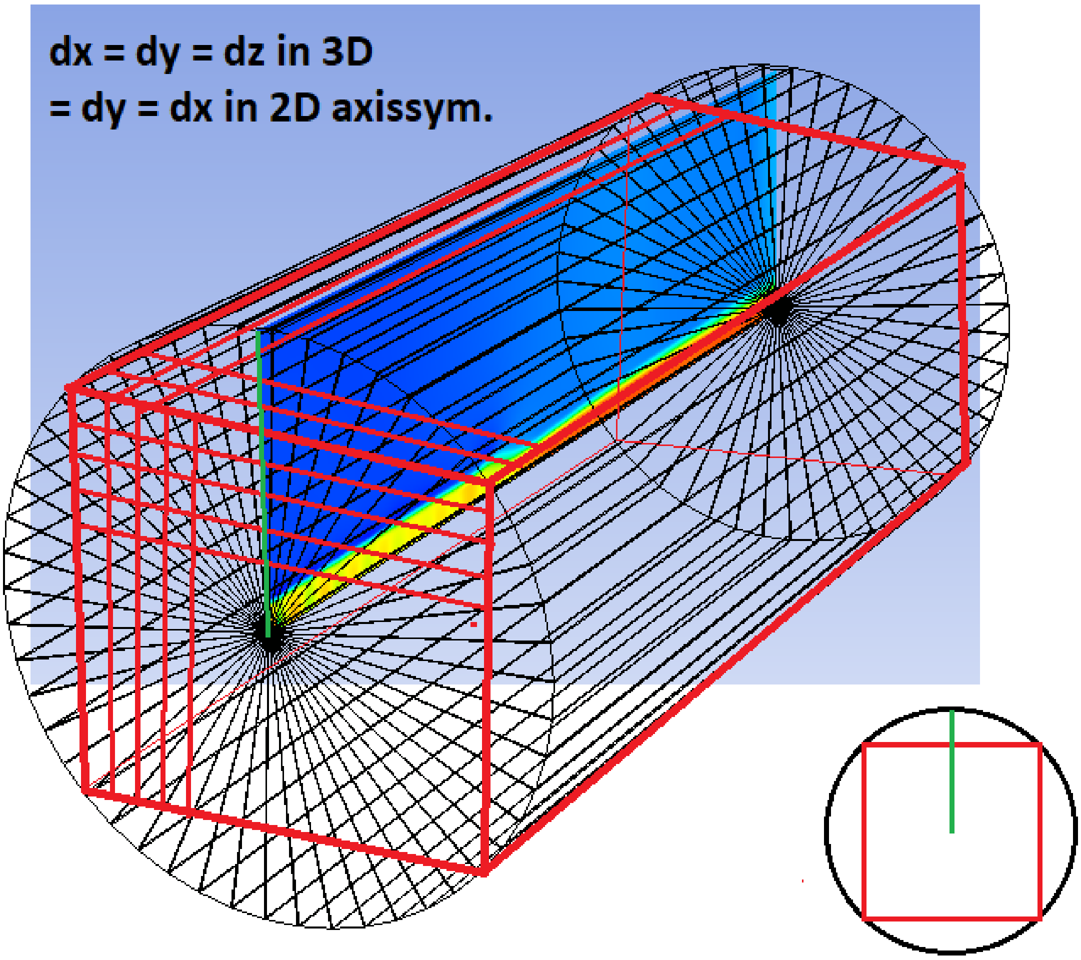

Figure 3.13: Visualisation of axisymmetric to 3-D transformation

An axisymmetric result of a 2-D simulation implies that the solution can be rotated over the axial direction to form a 3-D tube. The AER 3-D model, however, uses a rectangular grid, therefore the axisymmetric results are transformed using polar coordinates to coincide with the nodes of the required 3-D field. Then the results outside the red square are removed.

3.3.1. Wake results

The state of the flow field is shown below, Figure 3.14 shows the turbulent viscosity. The axial velocities start at $450 m/s$ which was the output of the GSP engine model and decrease slowly as the wake advects. The turbulent viscosity, however, grows as the free shear layer between the high-velocity jet and the lower-velocity free atmosphere increases in thickness. The static temperature field in Figure 3.16 shows the same structure as the axial velocity.

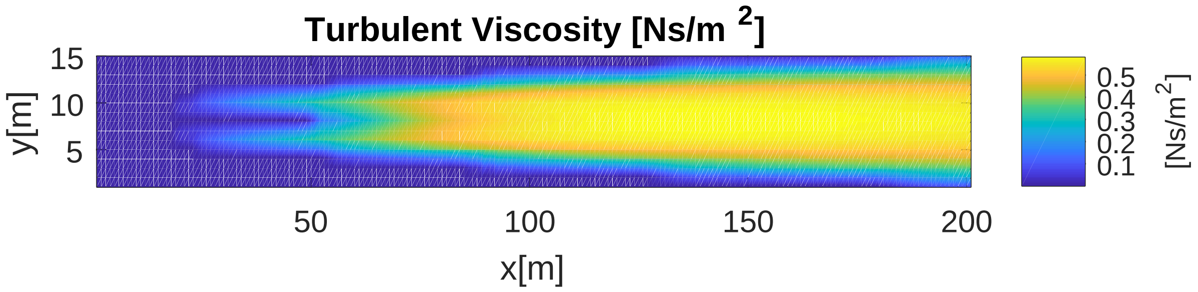

Figure 3.14: Turbulent viscosity field of the wake with outputs of the GSP Engine model as inlet boundary conditions

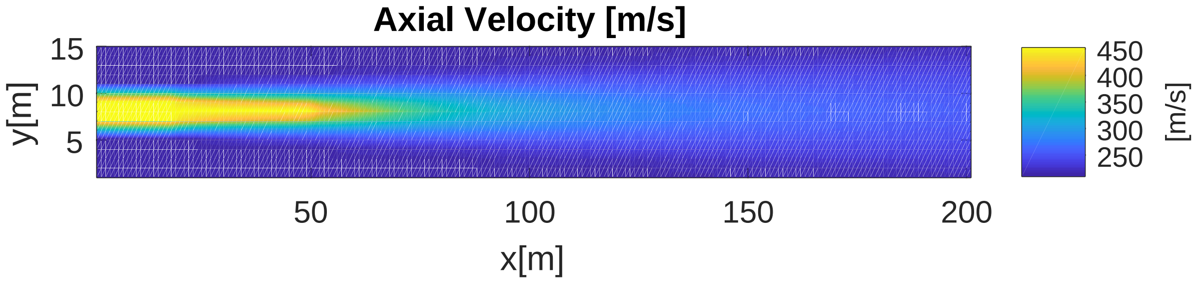

Figure 3.15: Axial velocity field of the wake with outputs of the GSP Engine model as inlet boundary conditions and a free-stream velocity of $210m/s$

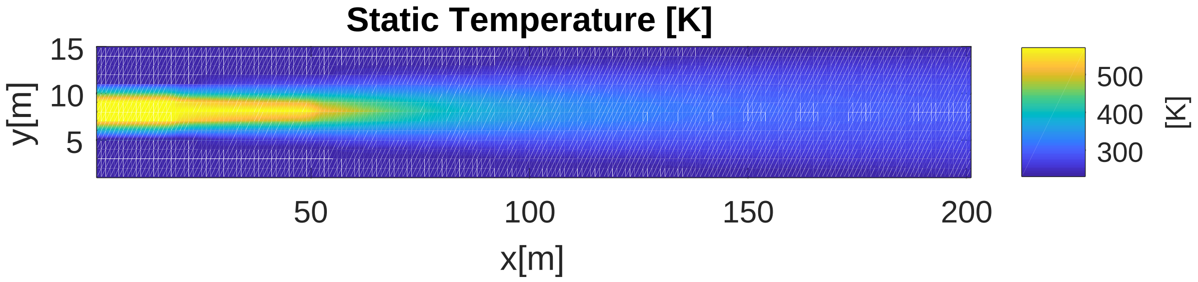

Figure 3.16: Static temperature field of the wake with outputs of the GSP Engine model as inlet boundary conditions and an ambient temperature of $218K$

3.4. AER 3-D: Advective Sectional Aerosol Model

The microphysical and fluid dynamics processes described in the previous chapter in a numerical form gives a simulation framework to investigate aerosol behaviour in aircraft plumes. This project will use the Atmospheric and Environmental Research (AER) sulphur model described by Weisenstein et al. [15] as a starting point for the simulation framework. This code was translated to MATLAB by Golja et al to the AER 3-D model. The aerosol mechanisms that are used in this model are coagulation, condensation/evaporation, homogeneous nucleation and sedimentation. The latter has been deemed negligible in the short timespans considered in this project in which turbulent effects of the wake dominate over sedimentation processes. The magnitude of the sedimentation velocity is in the order of 1-10 km per year [11], where the scope in this project is only seconds. This sectional model uses the approach to discretise the aerosol size distribution into sections or bins and the processes transfer the aerosols into the first bin, or from one bin to another.

In AER 3-D, the aerosol microphysics are defined by Hamill [25] as shown in Chapter 3. Sulphate aerosols are assumed to form through heteromolecular homogeneous nucleation of sulphuric acid and water vapour as the first nucleation mechanism explained in Chapter 2.1.3. Hereafter the size distribution is altered by condensation or evaporation of gaseous H_2SO_4 and coagulation, as indicated in Figure 2.1. The model assumes that all sulphate particles are liquid spheres with an equilibrated $H_2SO_4 - H_2O$ composition. This equilibrium is defined by the local temperature and relative humidity by Tabazadeh et al. [39].

The bin sizes used in the model range from $0.3nm$ to 3.2 μm over 40 bins where each bin's volume is double the volume of the previous bin as described in 2.1.1. The model also uses standard chemistry related to ozone compositions and sulphur chemistry. For the scope of this project, where large amounts of H_2SO_4 are injected, the choice was made to not include the chemistry as this is more commonly used when precursors of sulphuric acid are investigated that form H_2SO_4 eventually, while this method directly injects H_2SO_4.

The flowchart below shows the microphysical routines used in the AER 3-D model. The initial concentration of aerosols serves as the main input for the model whereafter the microphysical routines are called. First the condensation and nucleation routines, as explained in Section 2.1.4 and 2.1.3, are run multiple times to find an equilibrium in the amount of particles that condensate and nucleate. After the equilibrium is found, the coagulation routine from Section 2.1.5 calculates the amount of particles that merge and are shifted to larger bins. Once the microphysical routines are completed, the particles are advected using the transport equation that uses the diffusivity flow field to calculate new distribution of concentrations over bin sizes. Then the next time step uses this new concentration distribution over all the cells for the next iteration.

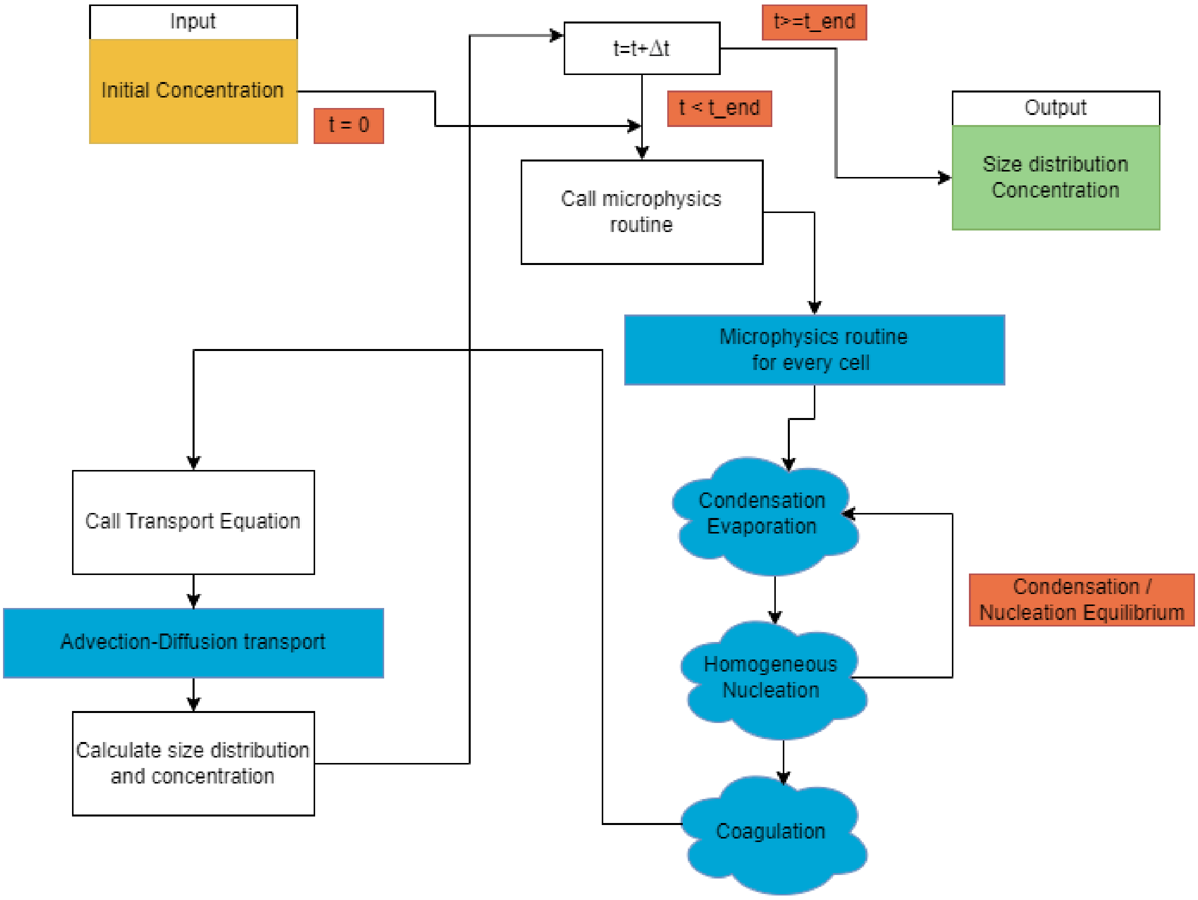

Figure 3.17: Flowchart of the AER 3-D model

4

Validating high velocity and high turbulent viscosity flow field in the AER 3-D model against comparable initial concentration box model studies

To validate the complete toolchain, we want to validate against the expanding Lagrangian box model of the TwO-Moment Aerosol Sectional (TOMAS) microphysics model [11] and box model for secondary aerosol formation using binary nucleation, brownian condensation and brownian and turbulent coagulation extended for plume dilulation [13] since they consider similar conditions of initial concentration and diffusivity. Since these use simple box models, the (advection) field needs to be adjusted to reproduce their spatial simplifications. The toolchain is therefore applied to quasi 1-D (Q1-D) domains. This Q1-D approach is first validated by comparing a Q1-D equivalent of the low velocity and low turbulence SCoPEx experiment, for which the AER 3-D model is developed, to its available 3-D results.

This chapter describes the three validation cases. First the code adjustments are shortly described to turn the 3-D model into a Q1-D model. Whereafter the 3-D results of the SCoPEx are compared [14] to the results of a Q1-D model to investigate the influence of the simplification of spatial variations. Then the box models of Benduhn et al. [13] and Pierce et al. [11] are investigated by comparing it to the results of the Q1-D model using their initial concentration of aerosols and turbulent diffusivity related to the increase of plume area. The validation of the last two cases is done to see if the toolchain can reproduce the trend in high initial H_2SO_4 concentrations and high diffusivity.

4.1. 3-D to Q1-D Code Adjustments

The first adjustment that is made is changing the model from a 3-D advection field to a Q1-D model. The code is adjusted to Q1-D where the width of the x-direction cells did not change and the area of the cell is defined as the area of a circle. This area was not kept constant resulting in a Q1-D model as shown below.

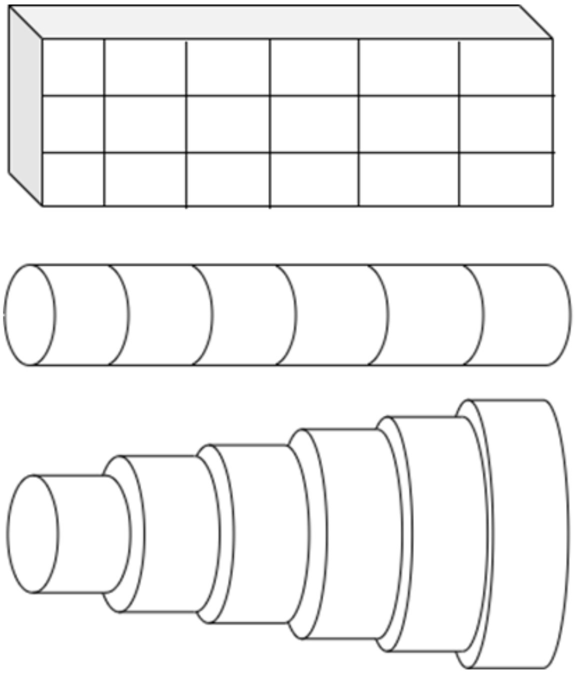

Figure 4.1: 3-D to Quasi 1-D

The second adjustment was done flow parameters like temperature and pressure which were considered constants in AER 2-D but are adjusted to be variable along the x-axis. Also the initial injection of H_2SO_4 had to be changed from 3-D to 1-D as shown in Figure 4.2. The 3-D model uses a 3-D Gaussian distribution of mass injection into the model grid whereas the Q1-D models take the integral of this 3-D gaussian distribution on x-constant planes. A smooth Gaussian distribution is used is to minimise the numerical truncation errors in the injection region.

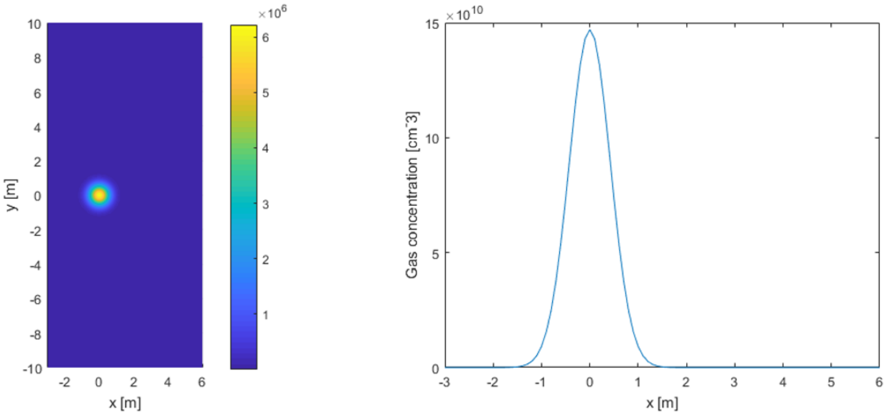

Figure 4.2: 3D domain to 1D and Quasi 1D

4.2. Comparison with AER 3-D low-velocity and low-turbulence case

Golja et al. considered a 3-D velocity field with H_2SO_4 injected near two propellers using the pre-mentioned microphysical mechanisms of AER 3-D for the SCoPEx experiment. The velocity and turbulent viscosity fields are shown below. They consider two injection configurations, scenario 1 is a single point injection between the propellers and scenario 2 considers 2 injection points from the center of each propeller.

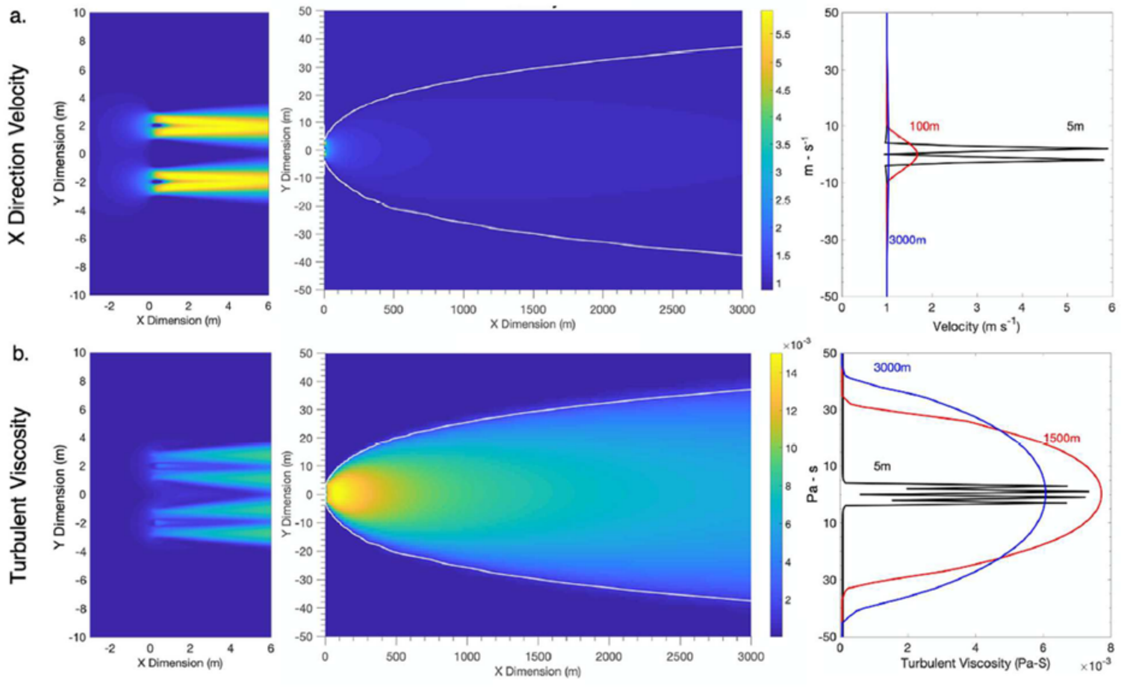

Figure 4.3: Domain of interest of the SCoPEx Stratospheric Balloon Experiment in AER-3D [14]

To compare both approaches, the quasi 1-D model uses the velocity and turbulent viscosity in the middle of the wake of the 3-D model. The area is calculated by inspecting all cells and investigate where the velocity is more than 1.1 times the background velocity ,and thus affected by the wake. This is visually presented by the white lines in Figure 4.4. The actual plot of the area increase is given in Figure fig:plumearea2.

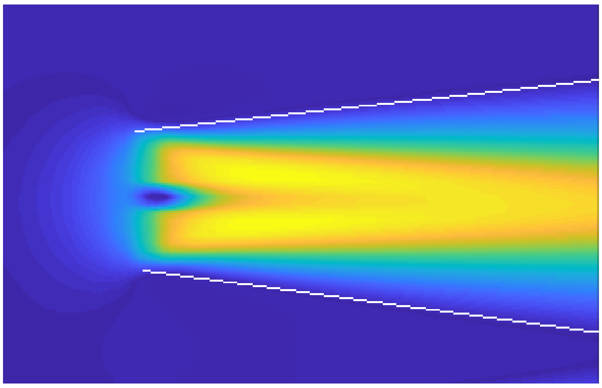

Figure 4.4: Plume area interpretation from available velocity field for the Q1-D SCoPEx case

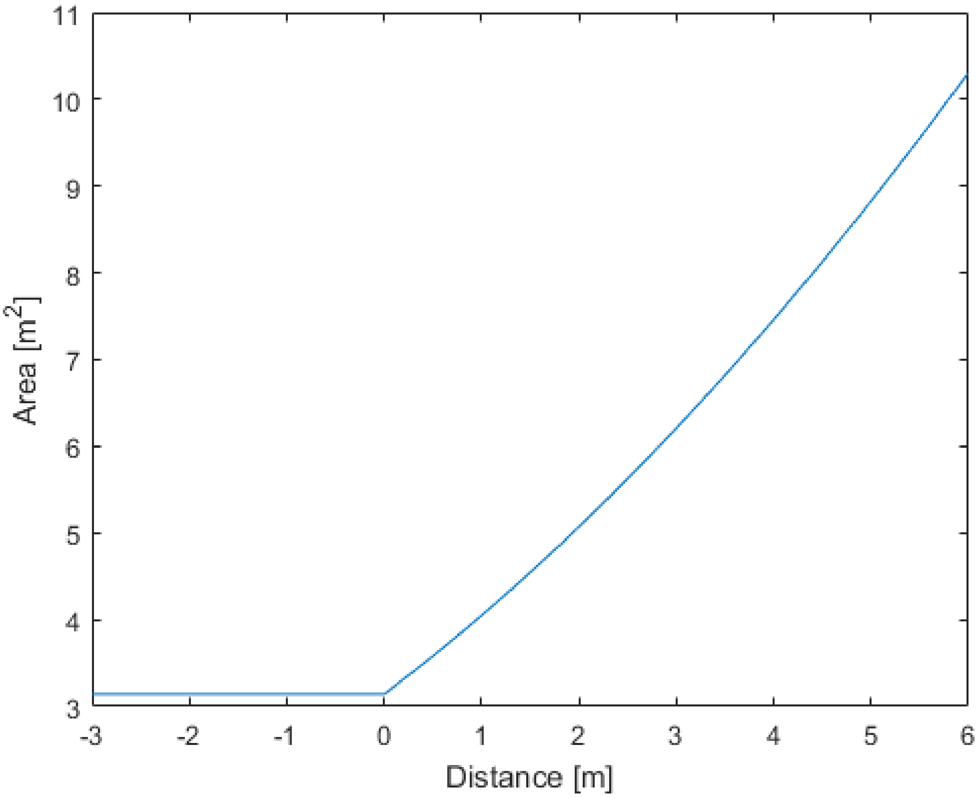

Figure 4.5: Plume area plot from available velocity field for the Q1-D SCoPEx case

Figure 4.6 shows the comparison of the initial few meters after injection.

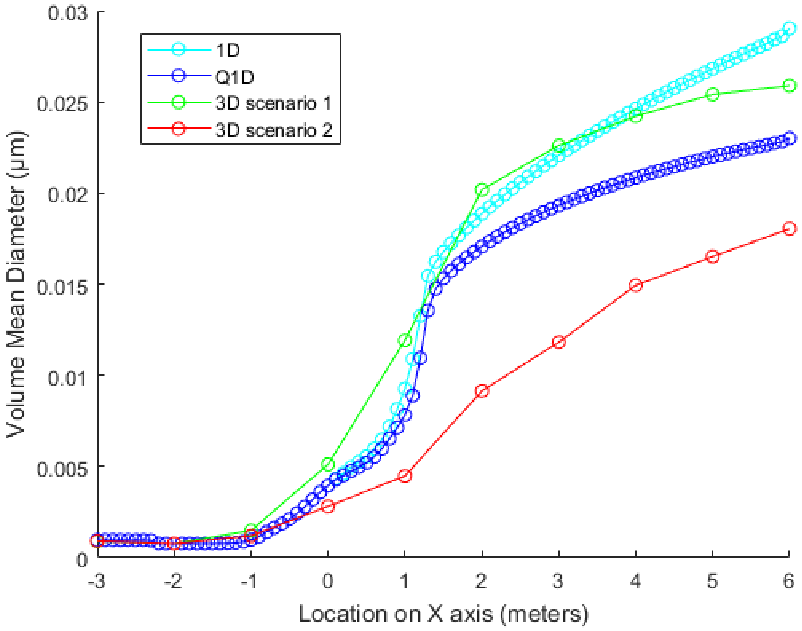

Figure 4.6: Volume mean diameter comparison between the Q1-D and AER 3-D model of the SCOPeX data in the initial meters after injection.

The red line in Figure 4.6 is the low-velocity and low-turbulence AER 3-D case while the blue line shows the Q1-D results. The volume mean diameter (VMD) of the Q1-D shows the same behaviour as the 3-D data but is larger than scenario 2. As scenario 2 divides the total injection mass over two wakes, a higher VMD is expected as the concentration is higher. The opposite is happening with Scenario 1 where the turbulent viscosity is lower and therefore diffuses the aerosols at the slower rate, keeping a higher concentration relatively to a higher diffusive wake. Figure 4.7 shows the more downstream behaviour of the volume mean diameter. Scenario 2 of the SCoPeX project where the initial concentration of H_2SO_4 gas is injected in the center of the propellers was considered most comparable as a Q1-D model can only inject in the middle theoretically.

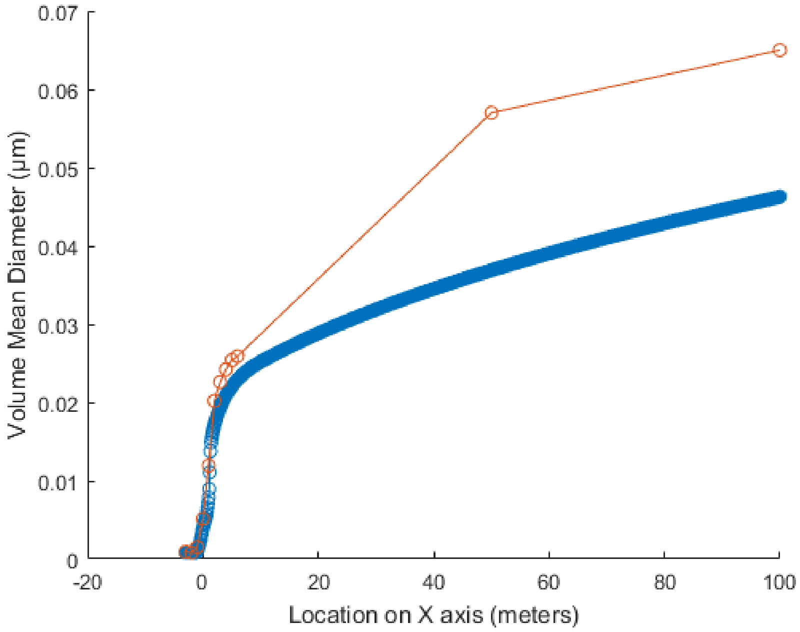

Figure 4.7: Volume mean diameter comparison between the Q1-D and AER 3-D model of the SCOPeX data up to 100 meters after injection.

In the initial few metres, the Q1-D model had larger VMD's than the 3-D scenario 2 but further downstream the 3-D model reaches higher diameters. Hunderd meters behind the injection the 3-D model reaches VMD of 0.062 μm whereas the Q1-D case calculated a VMD of 0.045 μm. Although the numbers do not coincide, the rate of change of the VMD in function of the location on the X-axis is similar. The discrepancy here can be related to an overestimation of the turbulent intensity for the Q1-D model, since the turbulent viscosity found in the centre of the 3-D model is used uniformly across the cross section of the Q1-D model.

4.3. Comparison with box model for secondary aerosol formation extended for plume dilulation

The goal of this research considers an aircraft engine plume. The case considered above in Section 4.2 is still lacking that. Therefore comparison to the box model for secondary aerosol formation using binary nucleation, brownian condensation and brownian and turbulent coagulation extended for plume dilulation is researched here. The idea of using turbulence from airplane turbines to optimize aerosol growth is investigated by Benduhn et al. as described in Chapter 1. They consider a box model where the plume dillution rate is defined by the diffusivity of the air and assumed to be constant during the simulation time. The aerosol microphysics are described in Benduhn [13] with parameterization of binary homogeneous nucleation by Vehkamäki et al. [20].

The area in the Q1D model is defined using the diffusivity parameter. In order to make our Q1D model input comparable to the expanding box model by Benduhn et al., we need to translate the initial concentration to an injection volume in our model. This is defined by

$$IV = y \cdot z \cdot n \cdot dx \tag{4.1}$$

where n is the number of cells over which material is injected. The time needed to fill this volume with velocity U is

$$dt = n \cdot dx/U \tag{4.2}$$

Therefore the number of molecules injected in the IV is

$$IR \cdot dt = IR \cdot n \cdot dx/U \tag{4.3}$$

Resulting in an IC for the 1D cases of

$$IR \cdot dt/IV = IR \cdot (n \cdot dx/U)/(y \cdot z \cdot n \cdot dx) = IR/(y \cdot z \cdot U) \tag{4.4}$$

4.3.1. Results

The part of the surface plot in Figure 4.8 that this project is interested in is the range between 10^{16} and $10^{17}/cm$ of initial H_2SO_4 and diffusivity ranging from 10^2 to $10^3 m^2/s$.

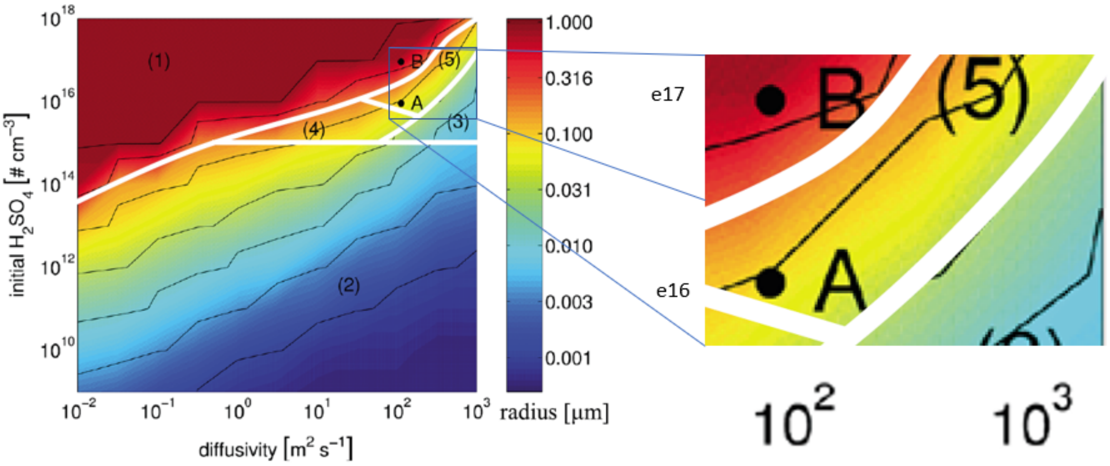

Figure 4.8: Area of interest of the results of the box model for secondary aerosol formation extended for plume dilulation, IC e16 to e17 and diffusivity e2 to e3

Figure 4.9 below shows the results of the Q1-D model. The same trend clearly shows in both surfaces. Where low diffusivity and high concentrations show the largest NMPR (number-median particle radius) of $0.4\mu m$ and high diffusivity and lower concentration result in smaller NMPR of $0.05\mu m$. The high concentration and diffusivity area (top right) shows NMPR of $0.3\mu m$ whereas the validation case's surface shows values closer to $0.1\mu m$. In the low IC and diffusivity region (bottom left) both surfaces show NMPR of $0.1 - 0.15\mu m$. It should be noted that due to the numerical bin distribution, the radii found are in close proximity even though it is double the size, this might explain the discrepancy in the high IC and diffusivity area.

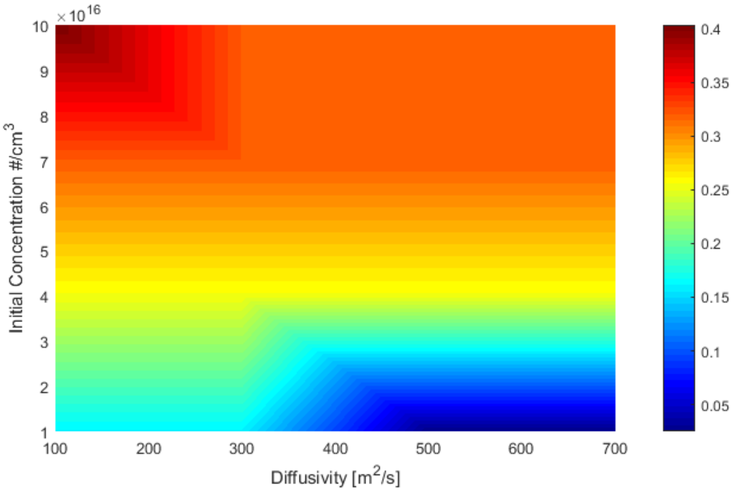

Figure 4.9: Number-median particle radius results from the Q1-D AER model.

4.4. Comparison with expanding Lagrangian box model of the TwO-Moment Aerosol Sectional (TOMAS) microphysics model

To increase confidence in the model, the Q1-D model is compared to the expanding Lagrangian box model of the TwO-Moment Aerosol Sectional (TOMAS) microphysics model. The previous case in Section 4.3 compares its data with this TOMAS model too and use different microphysical routines. These are point A and B on the particle radius surface plot in Figure 4.8. As this paper also shows particle number size distribution results, the Q1-D model is also validated with this paper. TOMAS uses 43 bins from $0.6m$ to $10m$ whereas the Q1-D model only uses 40 bins ranging from $0.3m$ to $3.2m$. The uncertainty for the plume dilution is investigated by a fast and slow diluting plume, however after 16 minutes the fast plume is switched to the slow diluting plume rates. The Q1-D results are compared to the slow diluting plume as particle number size distribution for this plume is found in literature.

4.4.1. Results

The time evolution of the peak decrease is shown Figure 4.10 and shows the converge to a steady-state. A non-linear decrease of the peak can be seen. It is therefore expected that the Q1-D model shows lower concentration but with the same median particle radius as the average remains in the same bin size.

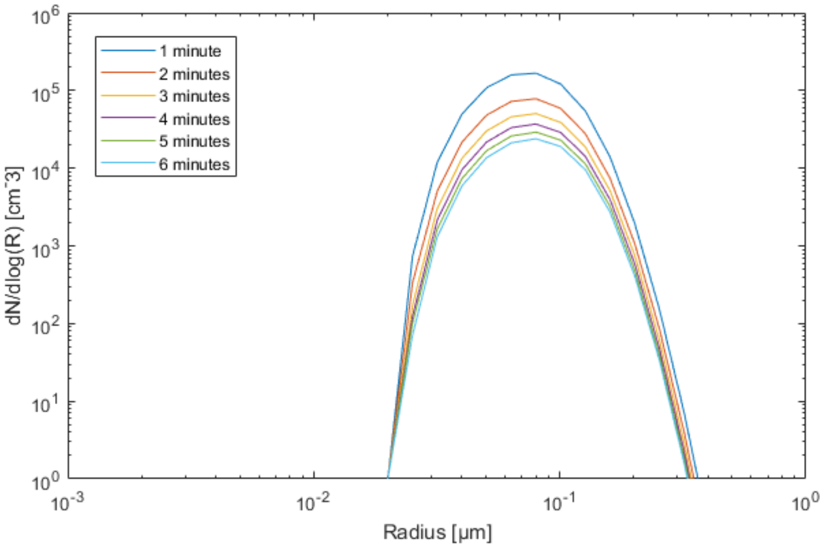

Figure 4.10: Time evolution of the size distribution in the Q1-D model

Figure 4.11 shows the comparison of the slow plume after an hour with the Q1-D AER 3-D results. The blue line represents the particle number size distribution with an IC of 10^{16} particles per cm^3. The red line represents the line from the data of the validation case for the same IC value of 10^{16} particles per cm^3. The Q1-D results show the same highest concentration of particles close to the $0.1\mu m$ bin comparable to the validation case. Also the concentration is in line with Pierce, both going up to $3 \cdot 10^4$ particles per cubic cm. However the validation data is 1 hour after injection but the Q1-D model only goes to 6 minutes after injection due to computational effort/time. The green line has an IC of 10^{17} and is shown to see the shift in size distribution with increase in IC.

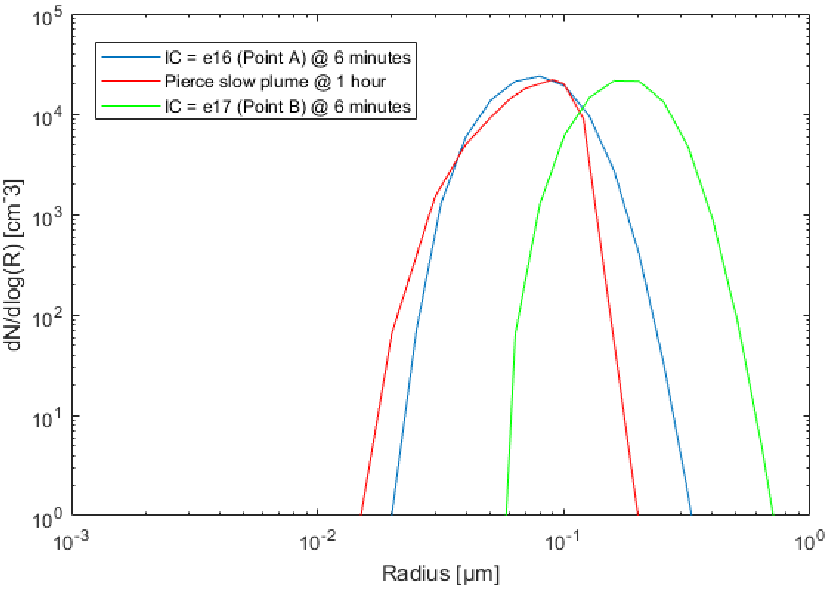

Figure 4.11: Particle number size distributions from expanding Lagrangian box model of TOMAS microphysics model and Q1-D AER model comparison

5

Integration of 3-D engine plume flow field in AER 3-D model

The toolchain is developed to use it for the study by Janssens et al. described in Chapter 1. This chapter introduces the flow case again and the initial concentration input for the research in Section 5.1 and the corresponding results in Section 5.2.

5.1. Flow case and Initial Concentration

The two parameters that have the highest influence on aerosol growth are the flow velocity and turbulent viscosity. Fields of the axial velocity and turbulent velocity of the aircraft engine plume are shown in Figure 5.1 and 5.2 respectively. The first 60 metres are shown, where the axial velocity of the outlet is 451 m/s and goes down to 300 m/s 60 metres after injection. The highest velocity can be found in the centre. The turbulent viscosity, which is the proportional to the gradient of the velocity, develops once the shear layer of the wake grows larger downstream reaching a maximum of 0.592 $kg/m \cdot s$.

The injection rate is set to 16111 $g/cm^3/s$ as described in Chapter 4 which corresponds to an initial concentration of $10^16[particles/cm^3]$ as given by the full injection scenario of Janssens et al.

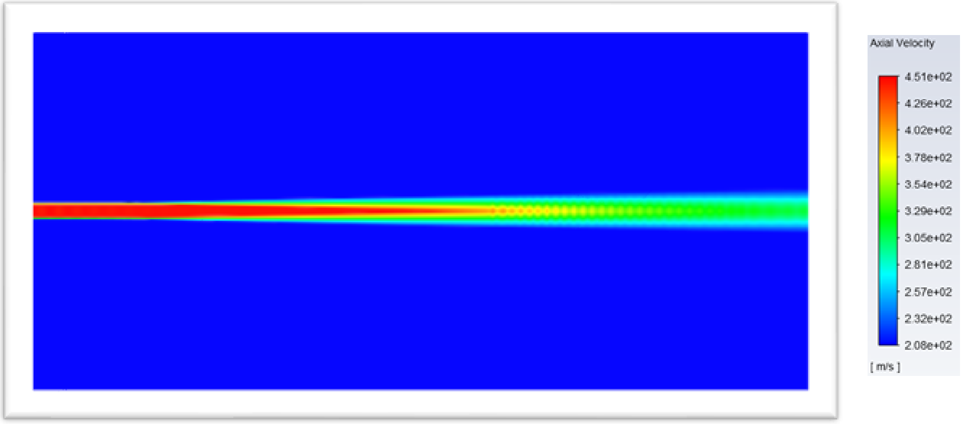

Figure 5.1: RANS results for the axial velocity component of the axisymmetric plume with velocity and temperature inlet boundary conditions derived from the GSP engine model and a free stream velocity of $210m/s$.

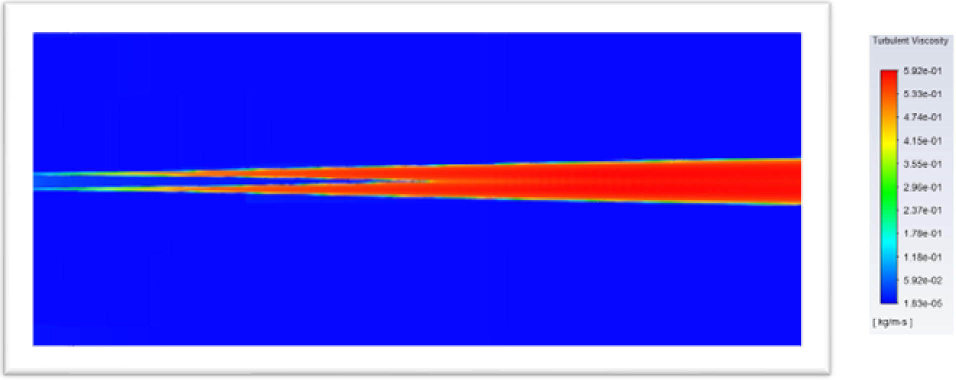

Figure 5.2: RANS results for the turbulent viscosity of the axisymmetric plume with velocity and temperature inlet boundary conditions derived from the GSP engine model and a free stream velocity of $210m/s$.

5.2. Results

In the 3-D axisymmetric flow field with AER 3-D microphysics model and advection scheme, the flow parameters determined using ANSYS serve as input for the advection scheme of the AER 3-D code. The initial concentration of gaseous H_2SO_4 that is researched here is $10^{16}cm^{-3}$, corresponding both to the point of interest in the box model for secondary aerosol formation by Benduhn et al. and the full injection scenario by Janssens et al. . Figure 5.3 shows the steady-state volume mean diameter of the aerosols XY-plane for z in the centre of the jet wake. Here, steady-state means that there is no more mass change in the bins for an advective iteration.

Once the turbulent viscosity reaches high enough values so that the aerosols are dispersed, the growth of the aerosol wake becomes apparent, around 50 meters behind the jet. The aerosols increase in diameter further downstream reaching values up to 0.13 μm.

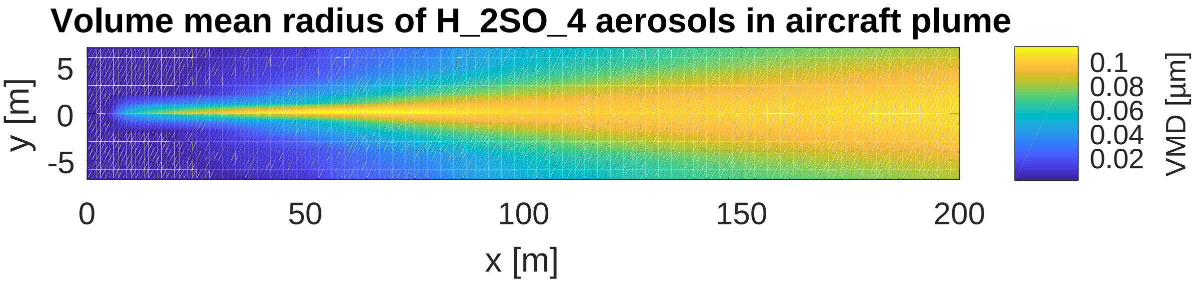

Figure 5.3: Volume mean diameter of H_2SO_4 aerosols in the aircraft plume for an initial concentration of $10^{16}cm^{-3}$

The gas particles that remain are visualised in Figure 5.4, the high concentrations of initial H_2SO_4 and the amount of water vapour available causes the gas to not be able to form particles straight away and keep condensing along the wake.

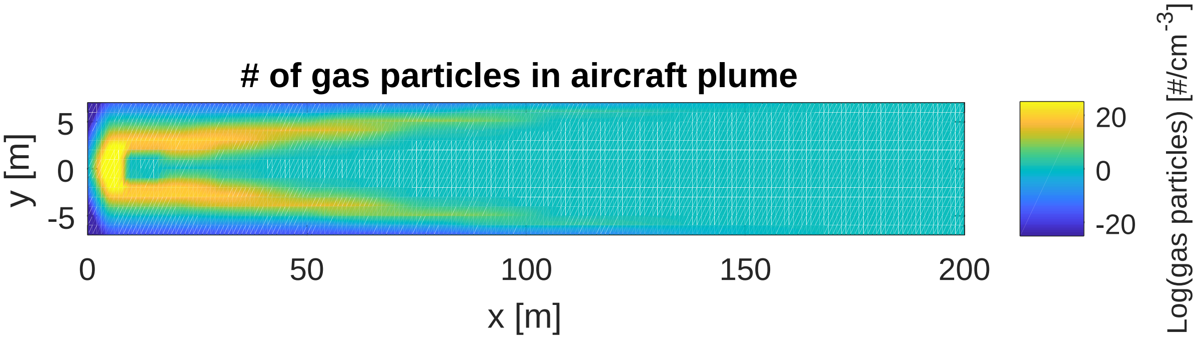

Figure 5.4: Amount of gas particles still present for an initial concentration of $10^{16}cm^{-3}$.

Figures 5.5 and 5.6 show the VMD and gas particles in an x-constant plane respectively. The largest diameter is always found in the core of the wake and shows an evenly distributed solution in radial direction. The maximum amount of gas particles moves radially away from the center as the injected H_2SO_4 moves downstream.

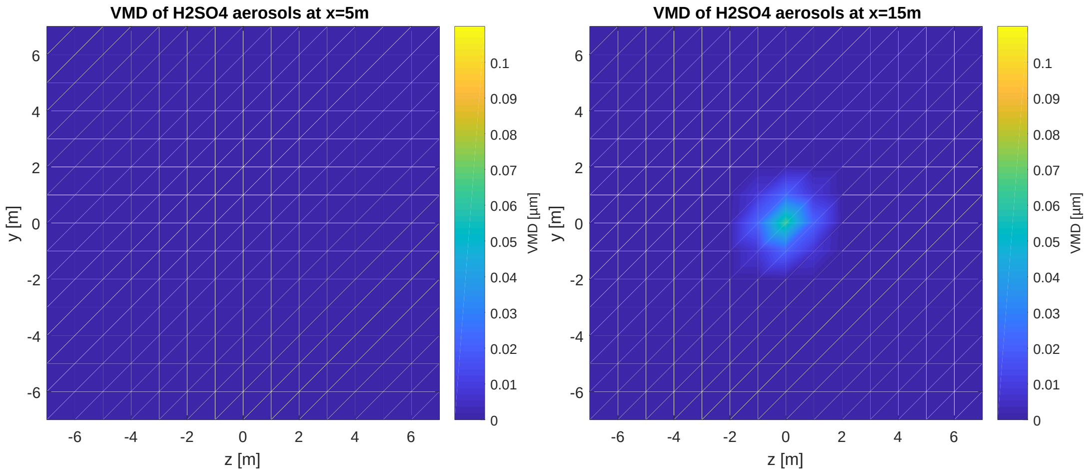

(a) x=5m **(b)** x=15m

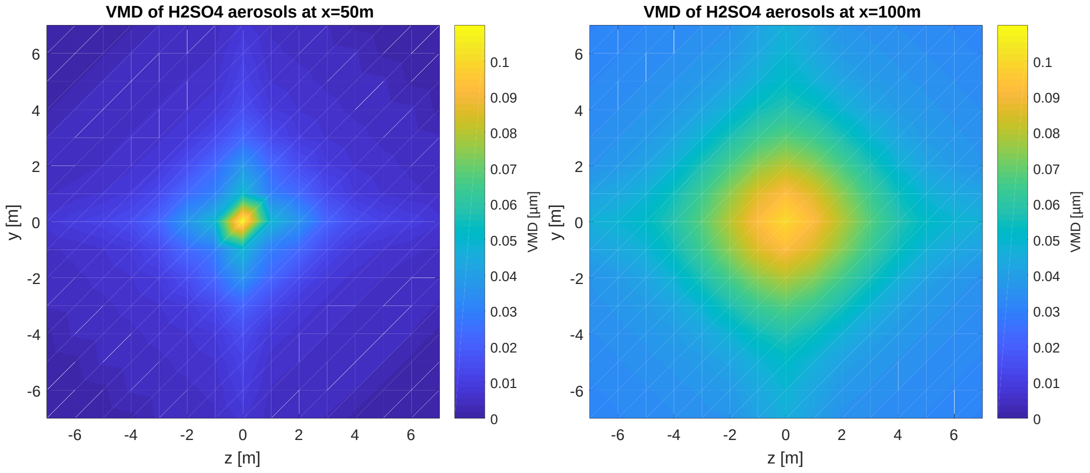

(c) x=50m **(d)** x=100m

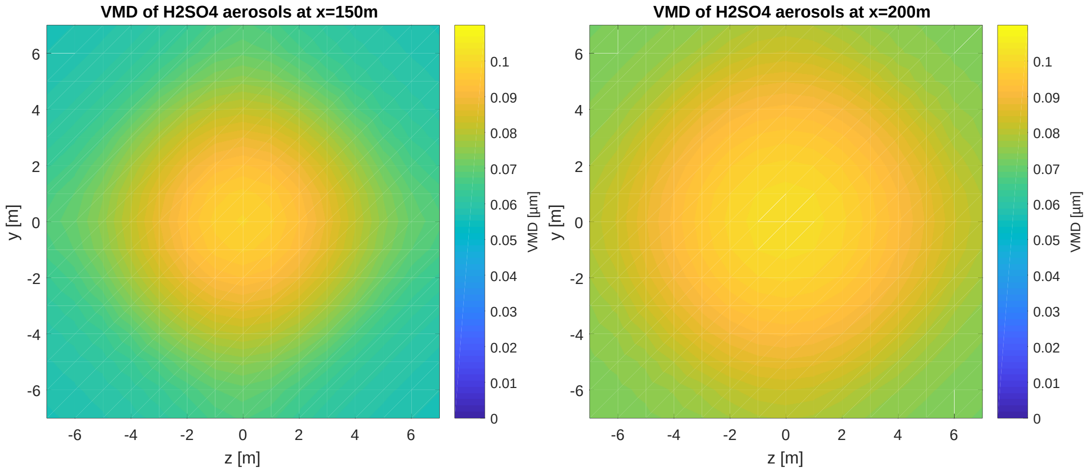

(e) x=150m **(f)** x=200m

Figure 5.5: Volume mean diameter of H_2SO_4 aerosols in the aircraft plume for an initial concentration of $10^{16}cm^{-3}$ along the x-axis

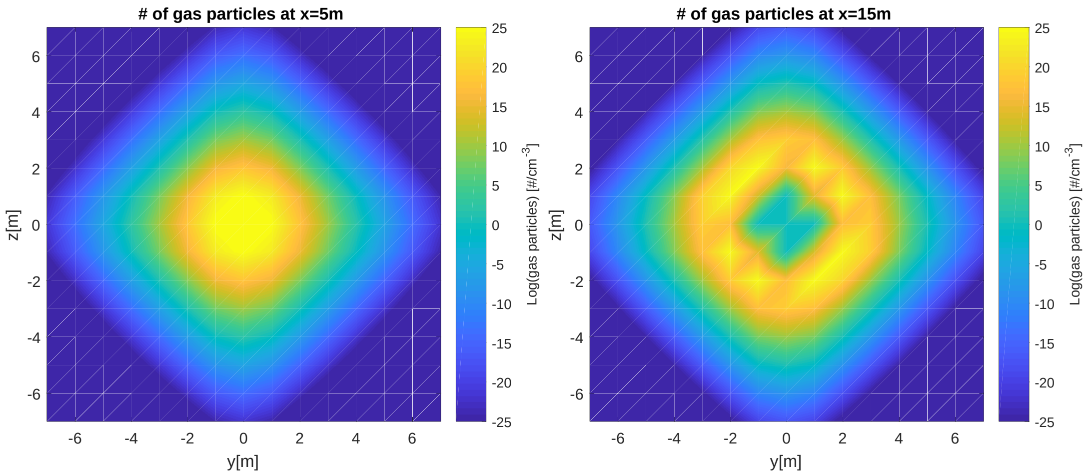

(a) x=5m

(b) x=15m

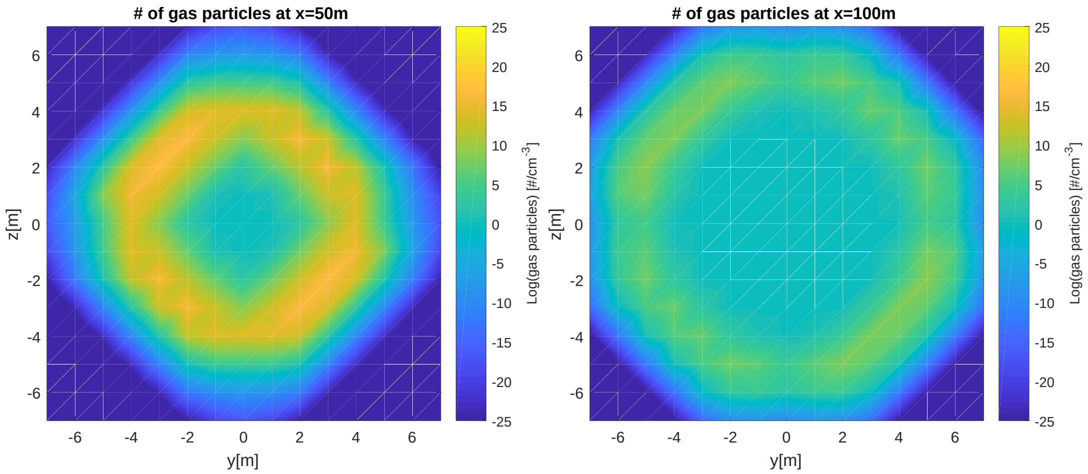

(c) x=50m

(d) x=100m

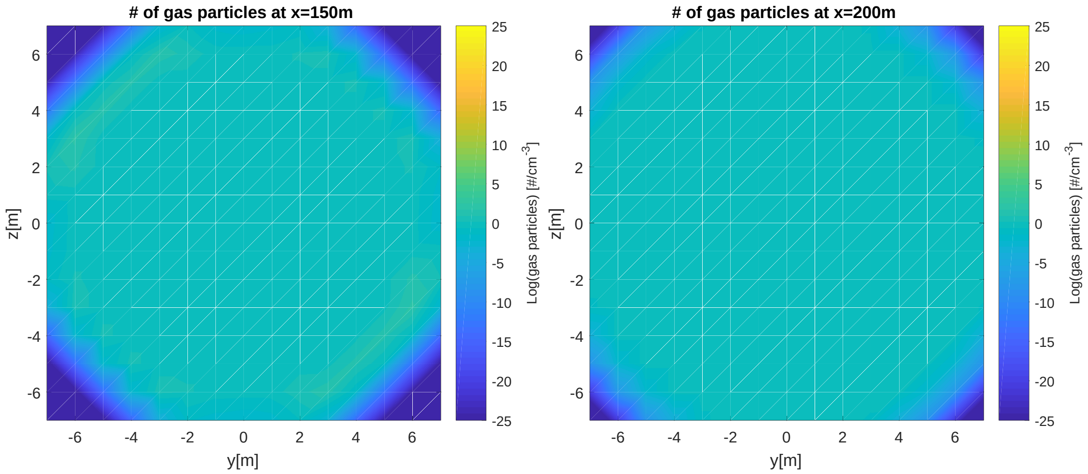

(e) x=150m

(f) x=200m

Figure 5.6: Amount of gas particles still present in the aircraft plume for an initial concentration of $10^{16} cm^{-3}$ along the x-axis

The microphysical rates of coagulation, condensation and nucleation are shown below. Coagulation is the main driver for growth of the aerosols once they are condensated and nucleated within the wake.

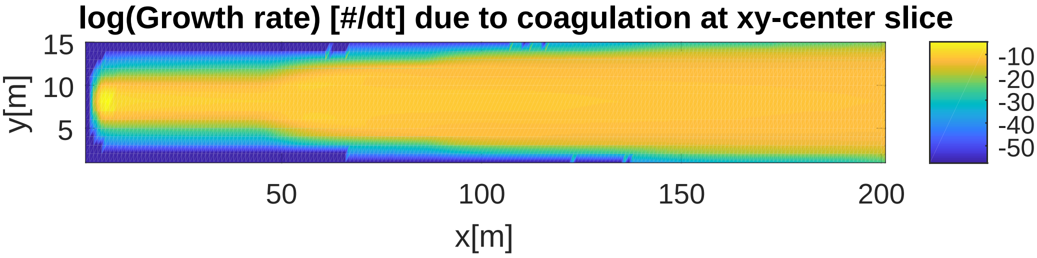

Figure 5.7: Coagulation rates in the wake for an initial concentration of $10^{16} cm^{-3}$

Condensation happens mostly right after injection and in the shear layer of the wake where gas is still present. The same can be said about nucleation, but is less so found in the shear layer where condensation has the upper hand compared to area of the injection. An observation when looking at the rates in different bins shown in the figures below is that nucleation only creates particles in the 1st bin and shows no nucleation to larger bins. In contrast, condensation happens in not only the first but all the way up to the 10th bin. This indicates that the population of aerosols is mostly dominated by larger particles that undergo condensation. This can be observed in conditions with high concentration of sulphate aerosols. According to Kerminen et al. [34], when the relative humidity is too low or the temperatures are too high, particles are also less likely to grow new particles through nucleation but rather through condensation.

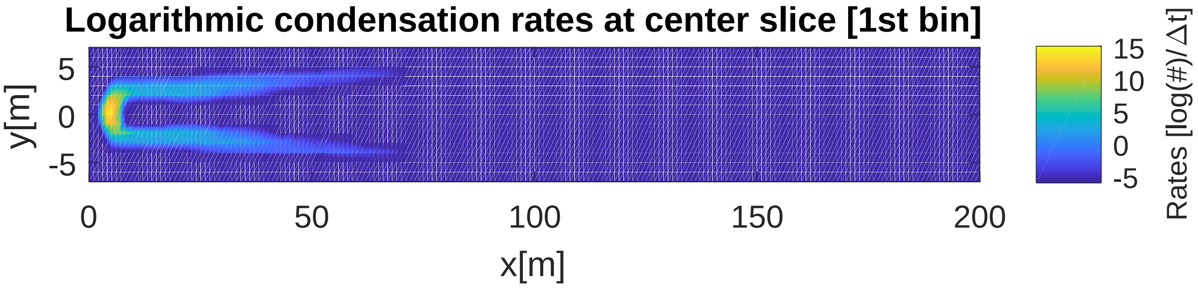

Figure 5.8: Condensation rates in the wake for an initial concentration of $10^{16} cm^{-3}$ [1st bin]

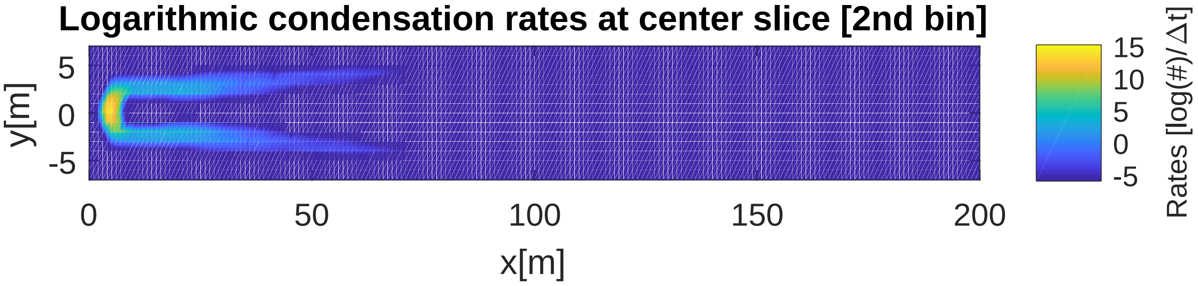

Figure 5.9: Condensation rates in the wake for an initial concentration of $10^{16} cm^{-3}$ [2nd bin]

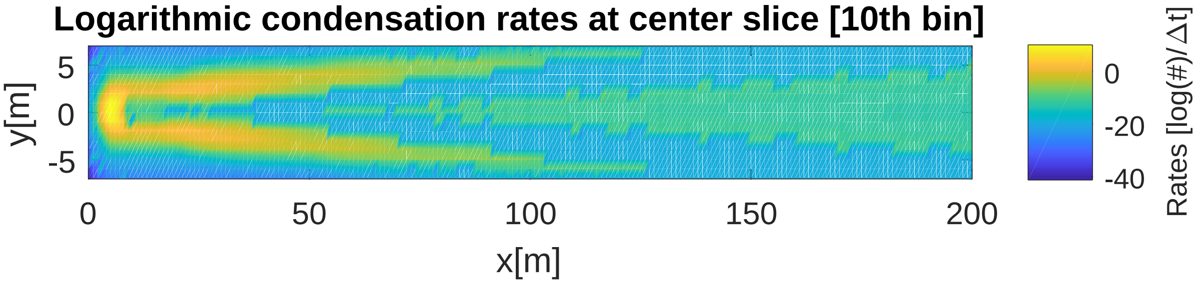

Figure 5.10: Condensation rates in the wake for an initial concentration of $10^{16} cm^{-3}$ [10th bin]

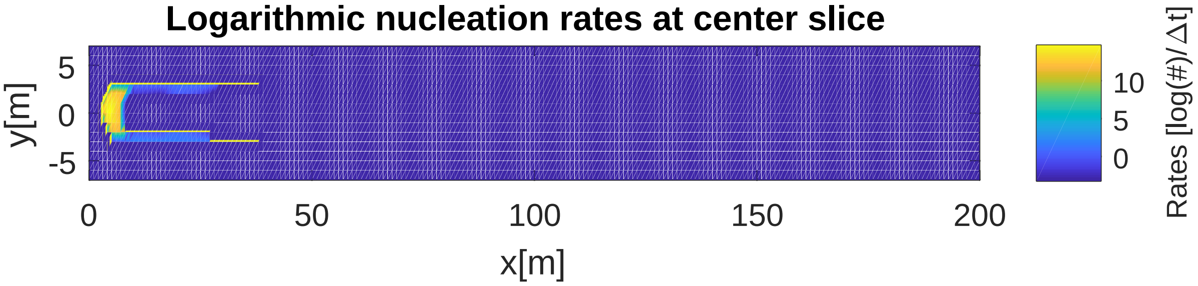

Figure 5.11: Nucleation rates in the wake for an initial concentration of $10^{16} cm^{-3}$ [1st bin]

When a gas particles is injected into the wake, it either condensates or nucleates almost instantaneously in the injection area if the water vapour concentration allows it. Particles that are diffused to the shear layer will condensate later as particles in the center of the wake. Once condensation and nucleation of the gas particles has happened in the first 50 meters of the wake, coagulation is the main driver of aerosol growth.

Figure 5.12 shows the comparison between the 3-D results and the Q1-D case 200 meters after injection. For the 3-D case, the same median radius method is used to calculate over the complete wake slice. The full 3-D case shows larger particles of 0.11 m whereas the Q1-D case has the most particles in the bin around 0.06 m. Another noticeable difference between the two graphs is the asymmetry of the 3-D case. An explanation is the large effect of turbulent viscosity creating more diffusion, giving the particles more room to grow with the available H_2O in the air. And as the centreline shows no turbulent viscosity initially, there may be a delay of this influence.

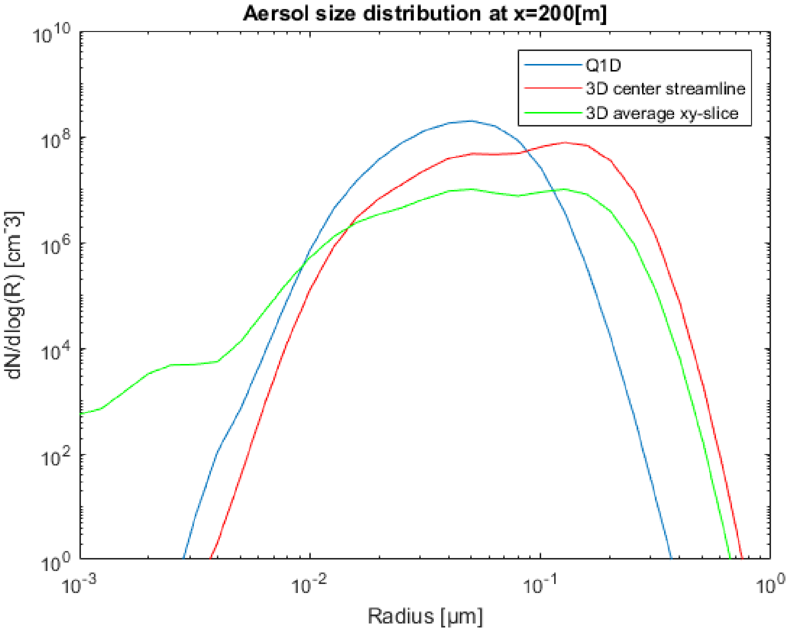

Figure 5.12: Comparison between the Q1-D and 3-D models for an initial concentration of $10^{16} cm^{-3}$

To determine the actual influence of a 3-D wake, Figure 5.13 shows the bin distribution in axial distance from the wake's centreline. The most and also largest particles are found at the centreline. As turbulence causes diffusion of the particles, both particle size and total number of particles decreases further away from the centreline. The simulated wake has a radius of 3-3.5 m which is in line with the minimal of particles found in the $3m$ radial distance region.

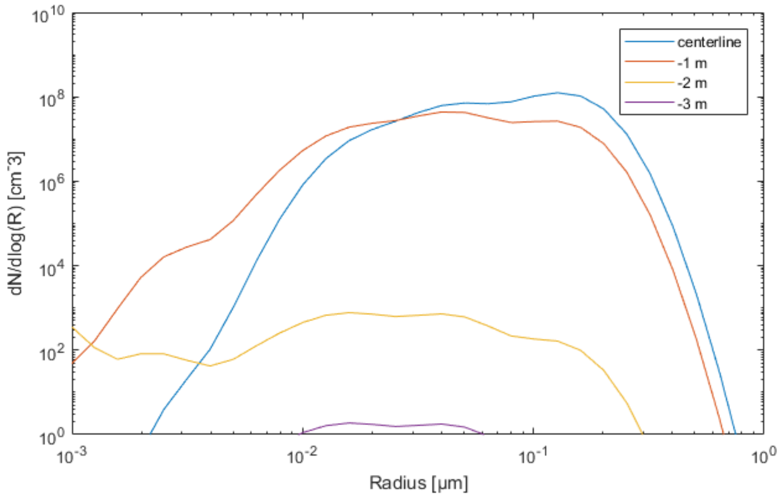

Figure 5.13: Bin distribution in radial distance from the wake's centreline for the 3-D case and an initial concentration of $10^{16} cm^{-3}$

To visualise the evolution of the particles in the wake, Figure 5.14 shows the bin distribution along the x-axis from 100m up to 200m after injection. When looking at the peaks of the bin with the most particles in it, a steady increase in size can be noticed. As the particles grow larger, the amount of particles declines.

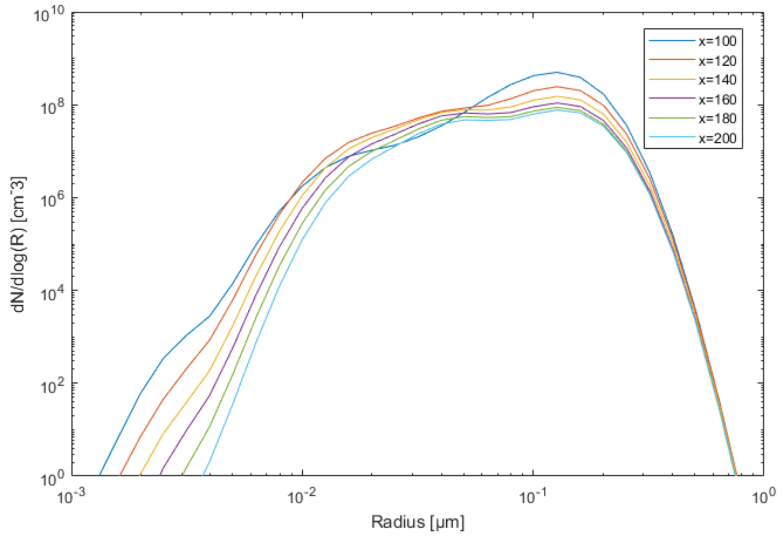

Figure 5.14: Bin distribution along the x-axis from 100m up to 200m after injection for the 3-D case and an initial concentration of $10^{16} cm^{-3}$

6

Conclusion and Recommendations

The main research goal of this thesis was to show if and how it is possible to achieve higher fidelity calculations with spatial variation on the behaviour of high concentration sulphate aerosols in an aircraft wake for the field of SAI research.

(RQ1.a) Up until now, only simple box models were found in literature that calculated average aerosol size in the presence of turbulence, which was idealised as an increase wake area with implied diffusion. Starting from these results, this study first investigated the performance of the aerosol microphysics model AER 3-D, versus the results obtained by two leading studies [11], [13]. The main difference between the AER model and the previous studies, is that an actual 3D flow field is used compared to a box model. Also, the microphysical routines used are based on different formulas found in the theoretical background section of this report. **(RQ1.b)** In order to facilitate the comparison of the box models with the AER 3-D model, a transformation was performed on the 3-D model, converting it into a quasi 1-D model. This transformation allows for a more meaningful and effective evaluation of the similarities and differences between the two modelling approaches. The validation with the SCoPEx experiment showed comparable results for the Q1-D and the 3-D models. **(RQ1.c)** The results comparing Benduhn et al. and Pierce et al. show that the AER 3-D model is capable of handling high initial concentrations of H_2SO_4, up to 10^{17} particles per cm^{-3}, resulting in larger particles in the areas of highest diffusivity. Similar results for the number-mean radius and size distribution as a function of initial concentration and plume growth rate are calculated, but the AER 3-D takes substantially longer to achieve the background concentration than the literature.

An axisymmetric engine wake field was then calculated in ANSYS with appropriate input boundary conditions which were obtained from simulations with the engine model GSP, configured to emulate an F118 engine.

(RQ2.a) The growth rates for one-way coupled results of the AER 3-D model show that condensation and nucleation are mainly found in the injection area and the boundary layer of the wake where gas remains present up to $100[m]$ after injection, whereas coagulation happens mainly inside the wake.**(RQ2.b)** The one-way coupled results show aerosols particles up to $0.12\mu m$ 200m after injection in the 3-D case, whereas the Q1-D case shows smaller particles around $0.06\mu m$. The differences are due to the inhomogeneous distribution of aerosols throughout the plume's cross-section, brought about by the advection of aerosols through the non-homogeneous flow field from the CFD calculation. The 3-D field also shows that H_2SO_4 particles as a function of distance to the center also varies up to 0.01 $\mu m/m$ away from the center. As the effectiveness of the aerosols is governed by the diameter, it is important to know which percentage of aerosols actually reach the diameter, and how this differs from a volume averaged calculation. **(RQ2.c)** The results demonstrate that areas with higher diffusivity correspond to larger particles. This observation can be attributed to the substantial influence of turbulent viscosity, which enhances diffusion and provides more space for aerosol growth through the available H_2O in the air. As turbulent viscosity reaches higher levels, causing aerosol dispersion, the growth of the aerosol wake becomes evident, particularly around 50 meters behind the jet.

These results show the importance of turbulence modelling and the coupling of it into the microphysical subroutines and advection scheme. Now that the framework has been set up, future research should include more sensitivity studies to flow parameters and a study on initial concentrations of H_2SO_4 to see what concentrations yields to the most favourable aerosol size. The complexity of the CFD and micro-physics can also be increased to investigate certain aspects that are not touched on in this thesis, including more accurate input conditions and microphysical routines that include ion-induced effects or including heterogenous microphysical calculations.

References

[1] Intergovernmental Panel on Climate Change. *The Earth’s Energy Budget, Climate Feedbacks and Climate Sensitivity*. Cambridge University Press, 2023, pp. 923–1054. DOI: 10.1017/9781009157896.009.

[2] David W. Keith. “GEOENGINEERING THECLIMATE: History and Prospect”. In: *Annual Review of Energy and the Environment* 25.1 (2000), pp. 245–284. ISSN: 1056-3466. DOI: 10.1146/annurev.energy.25.1.245.

[3] K. Caldeira and L. Wood. “Global and Arctic climate engineering: numerical model studies”. In: *Philos Trans A Math Phys Eng Sci* 366.1882 (2008), pp. 4039–56. ISSN: 1364-503X (Print) 1364-503X (Linking). DOI: 10.1098/rsta.2008.0132. URL: https://www.ncbi.nlm.nih.gov/pubmed/18757275.

[4] P. J. Rasch et al. “An overview of geoengineering of climate using stratospheric sulphate aerosols”. In: *Philos Trans A Math Phys Eng Sci* 366.1882 (2008), pp. 4007–37. ISSN: 1364-503X (Print) 1364-503X (Linking). DOI: 10.1098/rsta.2008.0131. URL: https://www.ncbi.nlm.nih.gov/pubmed/18757276.

[5] D. W. Keith et al. “Stratospheric solar geoengineering without ozone loss”. In: *Proc Natl Acad Sci U S A* 113.52 (2016), pp. 14910–14914. ISSN: 1091-6490 (Electronic) 0027-8424 (Linking). DOI: 10.1073/pnas.1615572113. URL: https://www.ncbi.nlm.nih.gov/pubmed/27956628.

[6] Ben Kravitz et al. “Geoengineering as a design problem”. In: *Earth System Dynamics* 7.2 (2016), pp. 469–497. ISSN: 2190-4987. DOI: 10.5194/esd-7-469-2016.

[7] D. K. Weisenstein, D. W. Keith, and J. A. Dykema. “Solar geoengineering using solid aerosol in the stratosphere”. In: *Atmospheric Chemistry and Physics* 15.20 (2015), pp. 11835–11859. ISSN: 1680-7324. DOI: 10.5194/acp-15-11835-2015.

[8] F. D. Pope et al. “Stratospheric aerosol particles and solar-radiation management”. In: *Nature Climate Change* 2.10 (2012), pp. 713–719. ISSN: 1758-678X 1758-6798. DOI: 10.1038/nclimate1528.

[9] Paul J. Crutzen. “Albedo Enhancement by Stratospheric Sulfur Injections: A Contribution to Resolve a Policy Dilemma?” In: *Climatic Change* 77.3-4 (2006), pp. 211–220. ISSN: 0165-0009 1573-1480. DOI: 10.1007/s10584-006-9101-y.

[10] David W. Keith and Douglas G. MacMartin. “A temporary, moderate and responsive scenario for solar geoengineering”. In: *Nature Climate Change* 5.3 (2015), pp. 201–206. ISSN: 1758-678X 1758-6798. DOI: 10.1038/nclimate2493.

[11] Jeffrey R. Pierce et al. “Efficient formation of stratospheric aerosol for climate engineering by emission of condensible vapor from aircraft”. In: *Geophysical Research Letters* 37.18 (2010), n/a–n/a. ISSN: 00948276. DOI: 10.1029/2010gl043975.

[12] M. Janssens, I. E. de Vries, and S. J. Hulshoff. “A specialised delivery system for stratospheric sulphate aerosols: design and operation”. In: *Climatic Change* 162.1 (2020), pp. 67–85. ISSN: 0165-0009 1573-1480. DOI: 10.1007/s10584-020-02740-3.

[13] François Benduhn, Jennifer Schallock, and Mark G. Lawrence. “Early growth dynamical implications for the steerability of stratospheric solar radiation management via sulfur aerosol particles”. In: *Geophysical Research Letters* 43.18 (2016), pp. 9956–9963. ISSN: 00948276. DOI: 10.1002/2016gl070701.

[14] C. M. Golja et al. “Aerosol Dynamics in the Near Field of the SCoPEx Stratospheric Balloon Experiment”. In: *Journal of Geophysical Research: Atmospheres* 126.4 (2021). e2020JD033438 2020JD033438, e2020JD033438. DOI: https://doi.org/10.1029/2020JD033438. eprint: https://agupubs.onlinelibrary.wiley.com/doi/pdf/10.1029/2020JD033438. URL: https://agupubs.onlinelibrary.wiley.com/doi/abs/10.1029/2020JD033438.

[15] Debra K. Weisenstein et al. “A two-dimensional model of sulfur species and aerosols”. In: *Journal of Geophysical Research: Atmospheres* 102.D11 (1997), pp. 13019–13035. ISSN: 01480227. DOI: 10.1029/97jd00901.

[16] N. A. Fuchs. *The mechanics of aerosols*. 1965.

[17] Helen M. Steele and Patrick Hamill. “Effects of temperature and humidity on the growth and optical properties of sulphuric acid—water droplets in the stratosphere”. In: *Journal of Aerosol Science* 12.6 (Jan. 1981), pp. 517–528. DOI: 10.1016/0021-8502(81)90054-9.

[18] Robert C. Reid. “Chemical engineers’ handbook, R. H. Perry and C. H. Chilton (eds.), McGraw-Hill, New York (1973).” In: *AIChE Journal* 20.1 (1974), pp. 205–205. DOI: https://doi.org/10.1002/aic.690200140. eprint: https://aiche.onlinelibrary.wiley.com/doi/pdf/10.1002/aic.690200140. URL: https://aiche.onlinelibrary.wiley.com/doi/abs/10.1002/aic.690200140.

[19] Glenn K. Yue and Adarsh Deepak. “Temperature dependence of the formation of sulfate aerosols in the stratosphere”. In: *Journal of Geophysical Research* 87.C4 (1982). ISSN: 0148-0227. DOI: 10.1029/JC087iC04p03128.

[20] P. Hamill and G. K. Yue. “A simplified model for the production of sulfate aerosols”. In: *Environmental and Climatic Impact of Coal Utilization*. Academic Press, 1980, pp. 255–274. ISBN: 0126463603.

[21] J. Zhao and R. P. Turco. “Nucleation simulations in the wake of a jet aircraft in stratospheric flight”. In: *Journal of Aerosol Science* 26.5 (1995), pp. 779–795. ISSN: 00218502. DOI: 10.1016/0021-8502(95)00010-a.

[22] Anni Määttänen et al. “New Parameterizations for Neutral and Ion-Induced Sulfuric Acid-Water Particle Formation in Nucleation and Kinetic Regimes”. In: *Journal of Geophysical Research: Atmospheres* 123.2 (2018), pp. 1269–1296. ISSN: 2169897X. DOI: 10.1002/2017jd027429.

[23] Joonas Merikanto et al. “Effect of ions on sulfuric acid-water binary particle formation: 1. Theory for kinetic- and nucleation-type particle formation and atmospheric implications”. In: *Journal of Geophysical Research: Atmospheres* 121.4 (2016), pp. 1736–1751. DOI: https://doi.org/10.1002/2015JD023538. eprint: https://agupubs.onlinelibrary.wiley.com/doi/pdf/10.

1002/2015JD023538. URL: https://agupubs.onlinelibrary.wiley.com/doi/abs/10.1002/2015JD023538.

[24] H. Vehkamäki. “An improved parameterization for sulfuric acid–water nucleation rates for tropospheric and stratospheric conditions”. In: *Journal of Geophysical Research* 107.D22 (2002). ISSN: 0148-0227. DOI: 10.1029/2002jd002184.

[25] Patrick Hamill, O. B. Toon, and C. S. Kiang. “Microphysical Processes Affecting Stratospheric Aerosol Particles”. In: *Journal of the Atmospheric Sciences* 34.7 (1977), pp. 1104–1119. ISSN: 0022-4928 1520-0469. DOI: 10.1175/1520-0469(1977)034<1104:Mpasap>2.0.Co;2.

[26] A.G. SUTUGIN N.A. FUCHS. “HIGH-DISPERSED AEROSOLS”. In: *International Reviews in Aerosol Physics and Chemistry* (1971). ISSN: 00747785. DOI: https://doi.org/10.1016/B978-0-08-016674-2.50006-6. URL: https://www.sciencedirect.com/science/article/pii/B9780080166742500066.

[27] N. Riemer, A. S. Wexler, and K. Diehl. “Droplet growth by gravitational coagulation enhanced by turbulence: Comparison of theory and measurements”. In: *Journal of Geophysical Research* 112.D7 (2007). ISSN: 0148-0227. DOI: 10.1029/2006jd007702.

[28] P. G. Saffman and J. S. Turner. “On the collision of drops in turbulent clouds”. In: *Journal of Fluid Mechanics* 1.01 (2006). ISSN: 0022-1120 1469-7645. DOI: 10.1017/s0022112056000020.

[29] M. R. Maxey. “The gravitational settling of aerosol particles in homogeneous turbulence and random flow fields”. In: *Journal of Fluid Mechanics* 174 (2006), pp. 441–465. ISSN: 0022-1120 1469-7645. DOI: 10.1017/s0022112087000193.

[30] M. Pinsky, A. Khain, and M. Shapiro. “Collisions of Small Drops in a Turbulent Flow. Part I: Collision Efficiency. Problem Formulation and Preliminary Results”. In: *Journal of the Atmospheric Sciences* 56.15 (1999), pp. 2585–2600. ISSN: 0022-4928 1520-0469. DOI: 10.1175/1520-0469(1999)056<2585:Cosdia>2.0.Co;2.

[31] L. P. Wang et al. “Theoretical formulation of collision rate and collision efficiency of hydrodynamically interacting cloud droplets in turbulent atmosphere”. In: *Journal of the Atmospheric Sciences* 62.7 (2005), pp. 2433–2450. ISSN: 0022-4928. DOI: Doi10.1175/Jas3492.1. URL: %3CGo%20to%20ISI%3E://WOS:000230962900007.

[32] G. K. Yue and A. Deepak. “Modeling of coagulation-sedimentation effects on transmission of visible/IR laser beams in aerosol media”. In: *Appl Opt* 18.23 (1979), pp. 3918–25. ISSN: 1559-128X (Print) 1559-128X (Linking). DOI: 10.1364/AO.18.003918. URL: https://www.ncbi.nlm.nih.gov/pubmed/20216726.

[33] Shivshankar Sundaram and Lance R. Collins. “Collision statistics in an isotropic particle-laden turbulent suspension. Part 1. Direct numerical simulations”. In: *Journal of Fluid Mechanics* 335 (1997), pp. 75–109. ISSN: 0022-1120 1469-7645. DOI: 10.1017/s0022112096004454.

[34] Yong Zhou, Anthony S. Wexler, and Lian-Ping Wang. “Modelling turbulent collision of bidisperse inertial particles”. In: *Journal of Fluid Mechanics* 433 (2001), pp. 77–104. ISSN: 0022-1120 1469-7645. DOI: 10.1017/s0022112000003372.

[35] Stephen R Turnock Anthony F Molland. *Marine Rudders and Control Surfaces*. 2007. ISBN: 9780750669443. DOI: 10.1016/b978-0-7506-6944-3.X5000-8.

[36] David C. Wilcox. “Comparison of two-equation turbulence models for boundary layers with pressure gradient”. In: *AIAA Journal* 31.8 (1993), pp. 1414–1421. ISSN: 0001-1452 1533-385X. DOI: 10.2514/3.11790.

[37] F. R. Menter. “Two-equation eddy-viscosity turbulence models for engineering applications”. In: *AIAA Journal* 32.8 (1994), pp. 1598–1605. ISSN: 0001-1452 1533-385X. DOI: 10.2514/3.12149.

[38] Anatolievna Lobanova Maria and Michailovich Tsirkunov Yury. “A study of flow and initial stage of water condensation in the exhaust jet of the aircraft turbofan engine”. In: *2nd ECCOMAS Young Investigators Conference (YIC 2013)* (2013). URL: https://hal.archives-ouvertes.fr/hal-00855869.

[39] Azadeh Tabazadeh et al. “A new parameterization of H2SO4/H2O aerosol composition: Atmospheric implications”. In: *Geophysical Research Letters* 24.15 (1997), pp. 1931–1934. ISSN: 00948276. DOI: 10.1029/97gl01879.